Terahertz radiation effects in quantum systems

Pardis Sahafi

Department of Physics
Royal Holloway, University of London

A thesis submitted to the University of London for the degree of Doctor of Philosophy

September 2018

Declaration

I, Pardis Sahafi, confirm that the work presented in this thesis is my own. Where information has been derived from other sources, I confirm that this has been indicated in the document.

Signed:

Date:

Acknowledgements

There are a great deal of people that should by all rights be acknowledged, but first and foremost is my Royal Holloway supervisor Dr. Vladimir Antonov. From introducing me to nanotechnology, to finally giving me the opportunity of participating in this PhD, it is no exaggeration to claim that my professional direction in life has very much been inspired by him.

My NPL supervisor Dr. Masaya Kataoka gave me the opportunity to work in a fantastic lab and with his world class group. He taught me a great deal about analysis and rekindled my interest in physics, and helped me overcome my short comings in knowledge, helping me become a better researcher. Special thanks to Dr. Stephen Giblin for all his input for the electron dwell time studies, as well as Dr. Jonathan Fletcher for all his help in general, especially concerning Labview programming.

Finally I must thank my family and friends. If I was to name all the individuals that helped me through this process I may have a longer acknowledgement than my thesis, although I must mention Ian Murray as without his help I would have never made it. I am truly grateful for all the support I had. Thanks to my Dad Fariborz, whose party trick of making his 5 year old recite parts of the atom, set me off on this journey. My Mother Maryam, who supported me throughout this PhD against her better judgement. My grandparents Hasan and Farangiz, who listen to my hours of explanation and feign interests for my sake. And finally, the deepest thanks to my little sister Neaky, for believing I was brilliant when I didn't, forgiving me for missing important occasions for work and always telling me that she was proud.

Abstract

I venture into the study of electron pumps in order to develop a more comprehensive understanding of the operation of these devices. We investigate the charging and relaxation of electrons within the dot . For research on charge relaxation of the dot we use devices where the point contact is coupled to the QD in order to probe the charge occupation of the dot. The devices are investigated and considered as possible single detectors of terahertz radiation. The phenomena related to propagating electrons through pumps were explored. We measured and analysed both the dwell times and the excitation states within the dot. The theoretical model of the device is discussed in relation to the study. The electron dwell times are mapped and we show the effects of applied magnetic field on them.

A multi-electron quantum dot is considered as a direct terahertz detectors in the investigation of the electron pump as an emitter. A few hundred electrons occupy the dot. The dot is charge excited by absorption of the terahertz photons. Thus it can be used as a sensitive terahertz detector. We study operation of the PC-QD devices and show successful use of the device for transmission and reflection terahertz imaging.

Contents

List of Figures

Chapter 1

Introduction

1.1 A brief discussion of unit standardisation

Metrology, the science of measurements [1], is a cornerstone of experimental science. The need to have a standardized international system of units (SI) is vital to accurate scientific study.

The National Physical Laboratory (NPL) is the UK's national metrological institute and tasked with maintaining unit standards. There has been an international effort to redefine many SI units as their original definitions are subject to error through natural degradation and in built errors. This has put many metrology laboratories across the world are working towards defining the units for each category.

So far resistance and voltage have been represented by quantum Hall effect [2] and Josephson effect [3] respectively.

The ampere is currently defined using ampere's law. In the metrological triangle it is currently not possible to measure it with the same degree of error by a couple of orders of magnitude so it is derived, rather than free standing [4, 5] , see figure 1.1.

At the moment current is in fact defined using the standard resistors calibrated using the quantum Hall resistance and the voltage from an array of Josephson Junctions [6–8]. Basing the Ampere on single electron transport [9] would be ideal, and the electron pump is good device to be used for this, transporting single electrons per cycle at frequency f. Here current is defined as $I = ef$, where e is electron charge.

At NPL, the Quantum Detection group has been working towards re-defining the current unit Ampere (A) since 1996. In their efforts to do so they have been utilising the electron pump in order to produce more and more accurate quantized current flow. This

has been done to an accuracy of $\approx 10^{-7}$ [10, 11].

However, the group realised that in order for their efforts to be successful they required a more in depth understanding of the energy transfer mechanisms used within the electron pump, since a device used to re-standardise the Ampere must fulfil two requirements. Firstly the uncertainty needs to be below 1 part in 10^6. Secondly current needs to be in the nA range. Smaller currents are impratical for metrological uses [8].

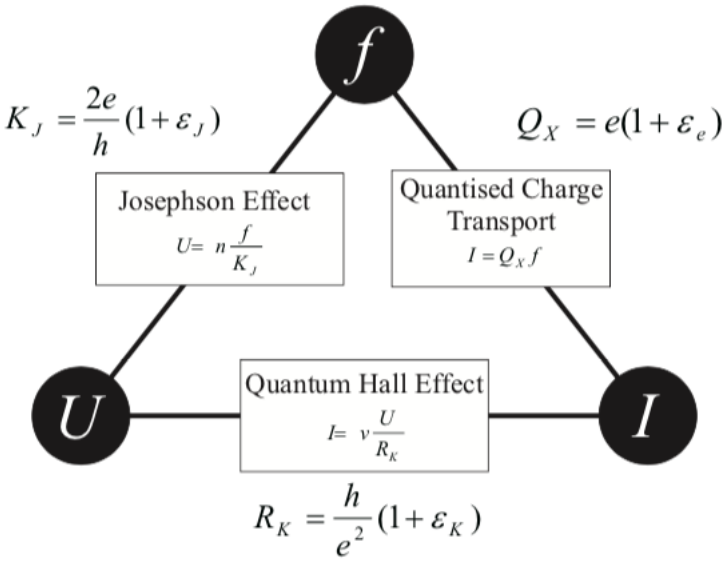

Figure 1.1: Schematic of the quantum metrological triangle experiments [12].

So far the later criteria is yet to be met, leading us to investigate the internal pump mechanics in order to utilise the new found knowledge to improve the current flow. This study provides foundational work required to investigate energy emission and detection studies within the electron pump.

And this is where we must start discussing terahertz, the key to allowing us to investigate the pumps fundamental properties.

1.2 THz radiation: An ever growing field

The research into terahertz radiation is a curious business. On the one hand it is a field filled with promising applications, whilst suffering from previously minimal research due to shortage of materials which can emit or detect terahertz, referred to by some as the terahertz gap.

This has gradually changed in the past 30-50 years, as the full scale of benefits

from this spectrum has become clear. Terahertz, encompassing frequencies between the infrared and the microwave spectrum, has a range of applications. From its non-ionising properties, making it ideal for medical imaging and a good replacement for x-rays [13–17], to applications in defence and security, accurately detecting harmful material [18, 19] and art provenance [20, 21] to name a few.

There are currently commercial detectors available detecting microwave radiation. However microwave photons have higher energy ranges (μ eV) in comparison to terahertz photons, which are far more challenging to detect (with an energy range of around meV) and require the use of devices based on quantum systems and measurements at low temperature.

This is where our electron pump studies overlap. By examining the electron pumps as both a single photon terahertz detector and emitter, we plan to conduct in depth studies of the energy transfer mechanisms prefered by the device at varying magnetic fields. In pursuit of this, other investigation other quantum systems will also be utilised to asist the electron pump investigation, amongst which are quantum dot (QD) based detectors, point contacts (PC-QD) and single electron transistors (SET-QD).

The aim of this work is to lay the foundation for more extensive research into the electron pump quantum system and building the necessary platforms (both in terms of equipment as well as software) to do so. We have succeeded in this endeavour.

Chapter 2

Survey of current technologies

Originally, the Oxford English dictionary, 1970, clarified the term terahertz as the frequency range of a HeNe laser [22]. Despite existing interest since the 1920s [23] , the first mention of terahertz was made in Fleming's 1974 paper [24], where it was mentioned in the discussion of the Michelson interferometer. Today, this term typically refers to frequencies in the range of 300GHz to 3THz. Initially the spectrum was only utilised in high resolution spectroscopy, but there has now been progress into use of this frequency range in commercial sensing, as well as imaging. This chapter touches on a few of the currently available technologies in this field, specifically work done on photon detection in this range.

2.1 Terahertz detection

The earliest investigations in this field began as a means of studying space and interstellar dust. Research suggests that 98% of emitted photons since the Big Bang are submillimeter and far infared in nature [25]. Many molecules, such as water and nitrogen, can be probed using terahertz radiation. Generally for detection of lower terahertz bands heterodyne detectors are preferable, and at shorter wavelengths direct detectors are far more sensitive.

Due to the low energies of terahertz waves ($\approx meV$), detection of terahertz wavelengths are generally challenging. Semiconductor based quantum devices have pushed progress in the field. The Quantum detector devices in presented in this body of work fall into this category, able to detect photons of a few meV. Since these devices work best at low temperatures, the improvement in low temperature measurements have also propelled current progress in this field.

There are plenty of examples of bolometric detectors, such as the superconducting bolometric detectors with single photon sensitivity reported by Santavica [26,27], useful for the search for earth-like exoplanets [28] and interstellar dust compositions. Table 2.1 lists examples of various terahertz detector devices and the frequencies they operate at [29].

There has been progress in research regarding resonant plasma mode excitations at cryogenic temperatures [30–33], and even HEMT operations as broadband terahertz detectors at room temperature [30, 31, 34, 35]. Si-MOSFET's have also shown themselves to be good terahertz detectors at room temperature for frequencies of $2.5THz$ as the NEP was one of the lowest for room temperature fast terahertz detectors [36, 37]. They have also been utilised for imaging applications [38].

In the challenging detectable regions of terahertz radiation, photons with energies of $h\nu <$ meV, are detected using semiconductor quantum devices [39–42] due to their low NEP which is less than 10^{-20} W/Hz$^{1/2}$ [43]. It should be noted that there have been many proposed detection schemes [39–42, 44–46].

Detectors for photon counting and imaging at low temperature have emerged [56–58] as well as devices for the generation and detection of single terahertz photons [59]. There has also been progress in utilising InGaAs Schottky barrier diode array detectors for compact terahertz line scanners in real time, with NEP of 106.6 10^{-12} W/Hz$^{1/2}$ [60].

It seems apparent that in a near future the terahertz range will no longer be deemed as the most neglected part of the spectrum.

Table 2.1: Table showing various THz detectors, and Frequency of detection [29].

Detector	Freq.(THz)	NEP	Year	Commercial	Ref.
Schottky	$0.11 - 0.17$	13.2	2007	VDI	-
barrier	$0.9 - 1.4$	113.7		-	-
diode (SBD)	$1.1 - 1.7$	113.7	-	-	-
SBD	0.86	42	2013	-	[47]
	0.28	290 pW		-	-
Photo conductive	$0.1 - 4.0$		2011	EKSPLA	-
Folded dipole antenna	$0.6 - 1.0$	66	2011	STM	-
FET	$0.7 - 1.1$	12 nW	2012	STM	-
VOx micro bolometer	2.5	37	2013	-	[48]
	2.5	3.6 μW	2015	-	[49]
Bolometer	4.25	24.7 pW	2013	INO	-
	2.54			-	-
Golay cells	$0.2 - 20$	10×10^3	2009	Microtech	-
Micro-bolometer	$1.0 - 7.0$	$< 100pW$	2014	NEC	-
$LiTaO_3$ Pyroelectric	$0.1 - 300$	96 nW	2014	Ophir Photonics	-
Pyroelectric	0.3, 1.0, 3.0	440	2009	QMC	-
Hot electron bolometer	0.89	7.4×10^3	2007	-	[50]
$Si_xGe_y : H$ micro-bolometer	0.934	200	2010	-	[51]
$\alpha - Si$ micro-bolometer	2.4	30 pW	2011	CEA-Leti	[52]
Nb_5N_6 micro-bolometer	0.1	398(2 mA)	2008	-	[53]
Vox micro-bolometer	2.8	35 pW	2008	Infrared Systems	-
Antenna QW cavity	$2.0 - 4.0$	32 pW	2014	CEA-Leti	[54]
VOx micro-bolometer	3.1	280 pW	2008	NEC	-
Folded dipole antenna	0.65	50	2010	STM	-
FET	$0.2 - 4.3$	28 (1.4 THz)	2012	-	[55]

2.2 Terahertz emission

Advances in optical rectification and photo-conduction techniques [61] have lead to creation of direct terahertz emission technologies with multi-mode lasers [62–64] i.e. sapphire-based lasers and Free-Electron Lasers (FELs). Table 2.2 [29], shows some of the recent advances in creating terahertz emitter.

Table 2.2: THz sources and their frequency of operation [29].

Source	Classification	Freq.(THz)	Year	Commercial	Ref.
Mercury	Thermal	Broadband	1950s	Bruker, Sciencetch	-
SiC globar	Thermal	Broadband	$< 1950s$		-
Cosmic background	Thermal	Broadband			-
BWO	Vacuum	0.65	2008	No	[65]
	electronic	0.1	2013	No	-
		0.2	2015	No	-
Free electron lasers	Vacuum	$0.1 - 4.8$	2001	No	[66]
	electronic	$1.28 - 2.73$	2007	No	-
Gunn diodes	Solid state	0.1	2007	No	[67]
	electronic	0.3	2014	No	-
Freq. multi. devices	Solid state	$0.7 - 1.1$	2016	Virginia Diodes	[68]
	electronic	$0.1 - 0.17$	2016		-
Gas	Lasers	$0.5 - 5$(discrete)	1970s	Edinburgh Inst.	[69]
Quantum cascade	Lasers	4.4	2002-06	No	[70, 71]
	Lasers	3.4	2014	No	[72, 73]
	Lasers	3.15	2014	No	-
	Lasers	3	2008-09	No	[74]
Diff. freq. generation	Lasers	5	2007	No	[75]
using 2 MIR QCLs		3.5	2015	No	-

In Gu's 1999 work, tunable dual wavelength external cavity laser diodes were discussed as a good source for tunable Continues Wave-THz (CW-THz) radiation [76]. This was followed by phase sensitive CW-THz imaging with diode lasers in 2004 [77].

The first terahertz Quantum Cascade Lasers (QCLs) operating in the terahertz

range were designed and simulated by Kohler [78]. There was a delay in it becoming operational, due to the impassible barrier in the phonon reststrahlen band, causing difficulty in expansion to lower emission terahertz frequencies [62]. Following this further studies were carried out on QCLs, showing their dependence on chirped superlattices [79].

For stronger CW-THz radiation, cuprate superconductors were used by Ozyuzer [80]. High temperature superconductor stacked Josephson Junctions are used to emit coherent terahertz frequencies the QCL photo-mixing technique cannot produce (0.5 - 1.4 THz) [62]. There has been recent progress in the study of Josephson Junction terahertz emissions, looking at high symmetry thermally managed BSCCO microstrip antenna [81]. There has even been a recorded emission of $2.4THz$ from a high temperature intrinsic Josephson Junction [82].

Going back to semiconductor contributions to terahertz emission and looking past Kohlers 2002 work with $GaAs\ AlGaAs$ heterostructure lasers [79], there has been progress in the field. Emission was utilised as a means of studying Si wafers surface potential using terahertz emission microscopy [83]. Etched vertical Si nanowires on 110 and 111 Si substrates also showed increased emission of terahertz when studied using terahertz time domain spectroscopy [84].

2.3 GaAs/AlGaAs heterostructure material for nano-devices

The $GaAs/AlGaAs$ semiconductor heterostructure is ideal for the formation of two dimensional electron gases (2DEGs). The AlGaAs has a wider band gap in comparison to the GaAs. The Fermi level can be shifted inside the gap by modulating the material doping. During growth of the heterostructure, a unified chemical potential is formed and an inversion layer is created at the interface, see figure 2.1. The 2DEG is formed by modulating the doping, and the charges are confined in the narrow channel into the substrate during processing [85, 86].

The particle in a box scenario can be replicated in the 2DEG by introducing barriers rising above the Fermi energy in which electrons maybe trapped, commonly referred to as quantum dots (QD). By simply adding the possibility of changing heights for one or both of these barriers, you then create what is commonly referred to as a dynamic quantum dot (DyQD). Once a QD enters a magnetic field (B-field), it can then be referred to as an artificial atom, as just like an atom it develops split energy states. Our ability to

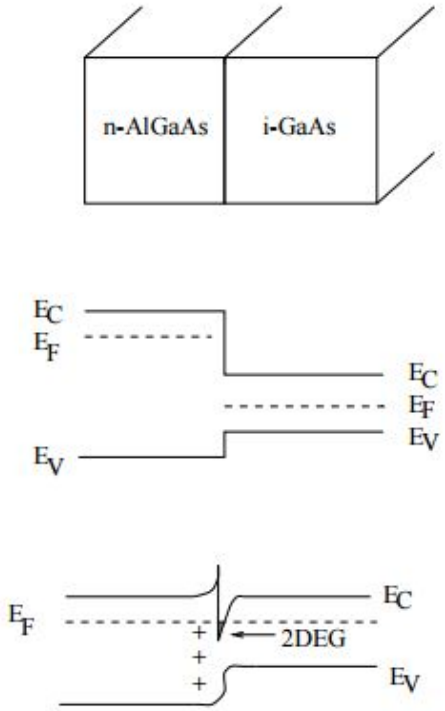

Figure 2.1: Band structure for AlGaAs/GaAs, before and after charge transfer between the two materials [87].

manipulate electron transport in these heterostructure and create systems with easy to modulate electron confinement is what makes GaAs/AlGaAs the ideal material to use as the base substrate for building the quantum systems used for our detection and emission experiments.

2.4 Summary

This chapter looked into the technological progress made in detection and emission of terahertz range photons. There has been great leaps in progress, especially using semiconductor quantum systems. In the following chapters we will focus on a few such systems, and their feasibility as terahertz sources and detectors.

Chapter 3

Study of single electron pumps

In our attempts to produce both emitters and detectors of terahertz radiation, we study electron pump devices, which are essentially dynamic quantum dots with a varying barrier allowing electrons to be "pumped" through the dot. These devices initially showed promise as both single photon emitters as well as detectors. Though neither application possibility was fully realised, the nature of electrons passing through these pumps were explored significantly, studying both their dwell times as well as their excitation states within the dot to clarify their applicability in the terahertz range. Work presented in this chapter is in order to develop the understanding required to design detectors and emitters based on these technologies.

Efforts have been made in developing a clearer quantum mechanical picture of the system. Data from various experiments, including this project, are being used to formulate a more comprehensive model.

3.1 Electron pump fabrication

Here we cover the fabrication methods used for electron pumps in this chapter as well as the QPC coupled electron pumps covered in chapter 4. Both are fabricated on the same substrate and follow similar steps. The only variance are small alterations made to the device designs.

The substrate is grown using molecular beam epitaxy (MBE) at Cambridge University. This technique, developed by Cho [88] in 1969, has the advantage of producing semiconductor substrates with nearly perfect vertical control of composition and doping down to atomic levels. In general within epitaxial processes a base substrate acts as a

crystal seed from which the rest of the wafer is grown. Two of the most common processes are Chemical Vapour Deposition (CVD) and Molecular-Beam Epitaxy (MBE). The MBE process involves one or more atomic or molecular thermal beams reacting with the substrate crystal under ultrahigh vacuum conditions. In this method there is control in both doping levels and chemical compositions of the grown base [85]. The design of the substrate is shown in figure 3.1. The wafer is the processed as schematically shown in figure 3.2.

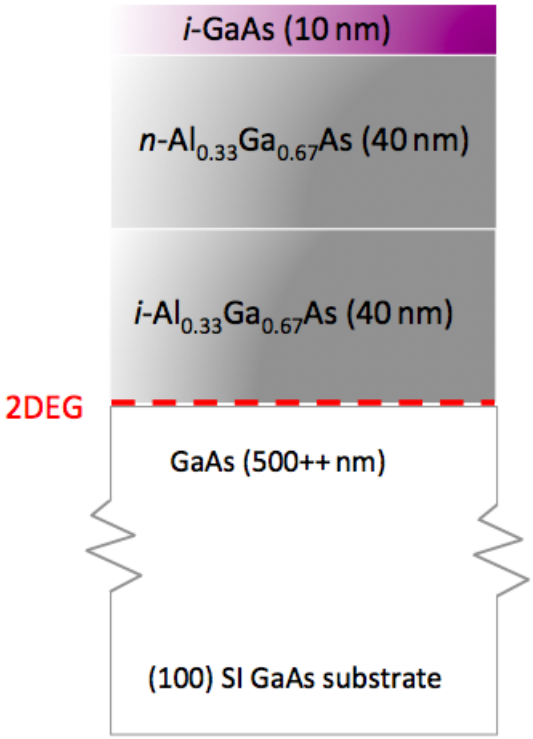

Figure 3.1: Cross sectional schematic of the electron pump GaAs-AlGaAs base substrate.

Using UV lithography (UVL) the mesa channel is created, followed by thermal evaporation of Ti/Au is used to create the outer metallic gates. The finer inner electron pump and QPC gates are then created by electron beam lithography (EBL) and thermal evaporation of Ti/Au. A large wafer containing dozens of devices is fabricated in the process.

In order to cleave the wafer into individual chips, the wafer surface is covered by a polymer layer (PMMA) to protect it from dust deposition during cleaving. After cleaving the sample, devices are dipped for 5 minutes in acetone and 30 seconds in isopropanol in order to remove the PMMA layer prior to bonding. The individual devices are bonded to

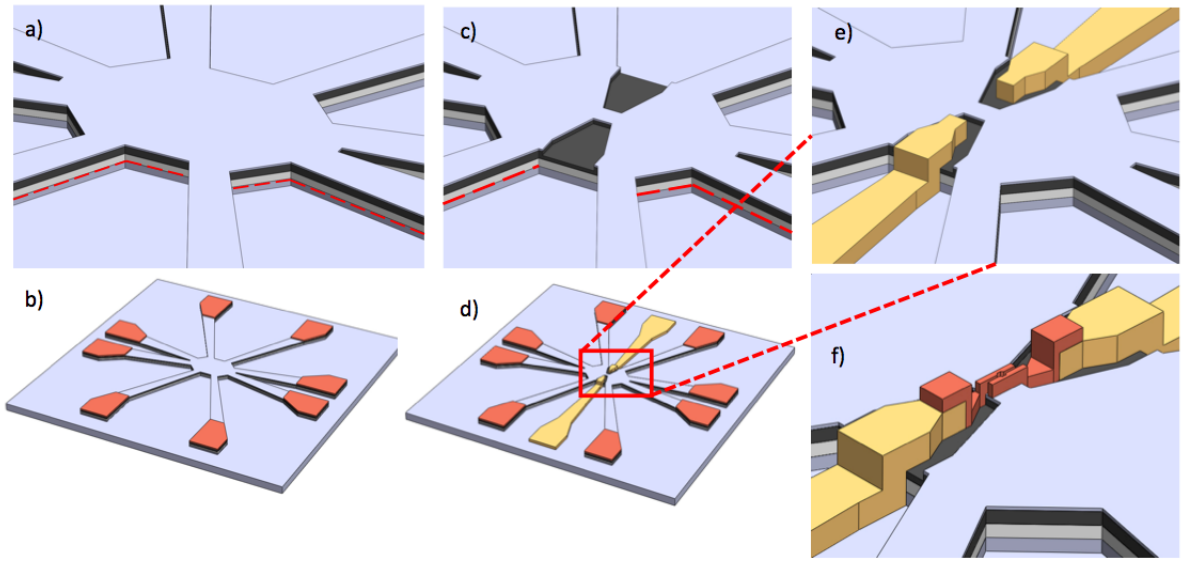

Figure 3.2: a) Substrate selectively etched up to the 2DEG, b) ohmic contacts deposited, c) sample selectively etched to create mesa channel, d) gates outer contacts deposited with e) showing a close up of where the pump gates will be. f) inner electron pump gates deposited after their shapes are defined using E-beam lithography [89].

the electron pump sample holder, shown in figure 3.12, using gold wires.

3.2 Fundamentals of the electron pump

To discuss electron pumps, we must conceptually understand the electron behaviour whilst trapped in a dynamic quantum dot. Since we are dealing with a quantum dot, it is worth noting that they are also commonly referred to as artifical atoms, were the nucleus potential has been replaced by another artificially created potential [90]. The dot has a more defined shape in the magnetic field, although that is not the only effect. Initially the electron pump can be modelled as single electron in a confined parabolic potential without considering the magnetic field. One can solve the Schrödinger equation with the potential of a nearly circular dot to be parabolic. The energy level for the first 7 electrons are equidistant, which is common for a parabolic potential.

To begin we will first look at a standard quantum dot with a parabolic potential. The electron behaviour in such a system can be described by the Darwin spectrum [91,92].

Using the transformations in [93, 94] the F-D Hamiltonian is written as:

$$\mathcal{H} = \hbar\Omega_+(a_+^\dagger a_+ + \frac{1}{2}) + \hbar\Omega_-(a_-^\dagger a_- + \frac{1}{2}) \tag{3.1}$$

where the eigenenergies are,

$$E_{n_+n_-} = \hbar\Omega_+(n_+ + \frac{1}{2}) + \hbar\Omega_-(n_- + \frac{1}{2}) \tag{3.2}$$

Ω is defined by the confinement frequency ω_0 and the cyclotron frequency ω_c:

$$\Omega_\pm = \Omega \pm \frac{1}{2}\omega_c \qquad\qquad \Omega = \sqrt{\omega_0^2 + \frac{1}{4}\omega_c^2} \tag{3.3}$$

This describes the behaviour of a charged particle in a parabolic potential in a magnetic field. Both Fock and Darwin solved the problem for the single electron trapped in a parabolic potential under applied magnetic field [91,92], and later the same problem in a zero confinement potential system was solved by Landau, leading to the development of the concept of *Landau levels* [95]

At low temperatures and high magnetic fields, the electrons occupy energy levels, which are degenerate and can only be resolved when the thermal energy is smaller than the energy level separation, $k_BT << \hbar\omega_C$, where k_BT is the thermal energy and $\hbar\omega_c$ is the cyclotron energy, with $\hbar\omega_c = (\hbar eB)/m^*$.

If the Zeeman effect is included into the model, each Landau level splits into a pair of level for different electron spins. However in our analysis we neglect the effect, since ω_0 is much larger than the Zeeman splitting [96].

Back to our electron pump system, the applied magnetic field separates the degenerate energy states in the QD. Figure 3.3 shows the theoretical model for a Fock-Darwin spectrum of a circular (symmetric) 2D quantum dot, where the potential $\hbar\omega_0$ is taken as 3meV [97]. This spectrum describes the energy levels in a QD at different magnetic fields.

The eigenenergy of an electron in a two dimensional QD in the presence of a magnetic field, B, is described by the formula;

$$E_{n,l} = (2n + |l| + 1)\hbar\sqrt{\omega_0^2 + \omega_C^2/4} - l\hbar\omega_C/2 \tag{3.4}$$

Where $\hbar\omega_0$ refers to the electrostatic confinement energy, n refers to the radial quantum number, l is the angular quantum momentum. This equation can be derived from equation 3.1. For GaAs $\hbar\omega_c = 1.76$meV at a magnetic field of 1T.

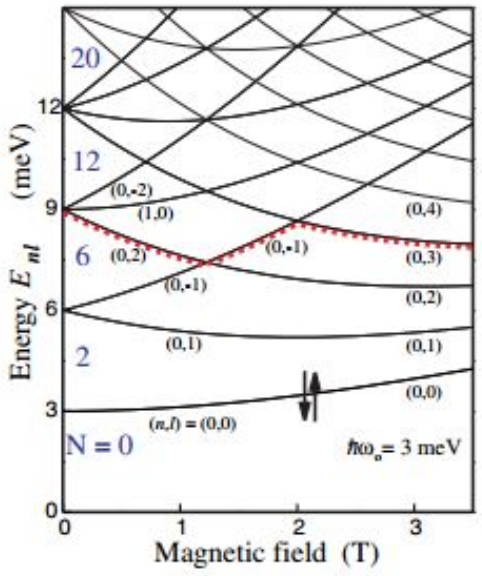

Figure 3.3: Single particle states in magnetic field, plotted for a potential of 3meV, including two fold spin degeneracy [97].

So far the system has been discussed as a quantum dot, but further considerations must be made since the system is a dynamic quantum dot. A confinement with varying barrier heights. This consideration is made and described by the Decay Cascade model [98, 99].

The Decay Cascade Model describes the occupancy of the dynamic quantum dot [98]. The rate of change in occupation of the QD, $dP_{n(t)}/dt$, is related to the decay rate of the charge states with n electrons ,Γ_n, in the dot.

$$dP_{n(t)}/dt = -\Gamma_{n(t)}P_{n(t)} + \Gamma_{n+1(t)}P_{n+1(t)} \tag{3.5}$$

Where P_n refers to the probability of an electron to remain in the dot. The occupancy is a sum of loading, $\Gamma_{n+1(t)}P_{n+1(t)}$, and unloading, $\Gamma_{n(t)}P_{n(t)}$, the dot. There are many solutions to this function, as well as many states that the electrons can end up occupying.

An illustration of this behaviour is shown in figure 3.4.

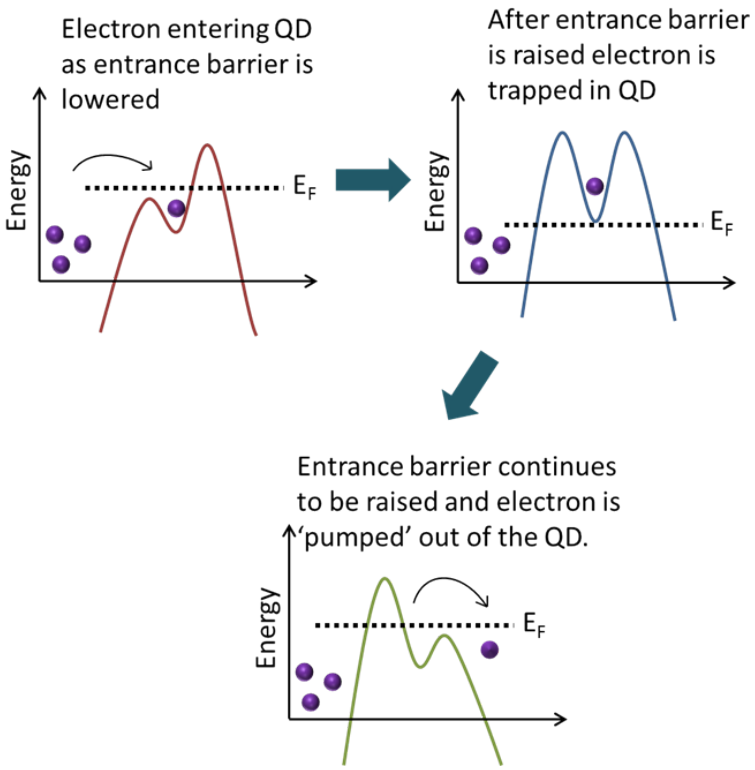

Figure 3.4: A simple semi-classical schematic of the e-pump operation in one pump cycle, excluding any back tunnelling or decay [99].

The entrance barrier is periodically lowered below the Fermi energy, allowing some electrons to enter the dot from the source, as shown in figure 3.4. As the barrier starts to rise, some of the electrons in the dot back tunnel into the source.

The outcome of this leads to a predictability in the number of electrons left behind in the dot, once the barrier is lifted above the Fermi level. When the two barriers are of

similar heights, the tunnelling rates out of the dot are very small. It is assumed that the majority of electrons remain trapped. Whilst the input barrier continues to rise, the shape of the potential well changes, encouraging electrons to forward tunnel into the drain.

Electrons may enter a higher energy level rather than the ground state when tunnelling into the dot. The electron trapped at the excited level may later relax to the ground state after releasing excess energy. This energy could be released in the form of phonons or photons.

Once again, to understand these transitions inside a dynamic QD, we should consider the transport, tunnelling and transitions in a static QD. Particularly the process of relaxation is interesting under the condition of resonance illumination [100]. The F-D spectrum has two dipole-active optical transitions for frequencies $\pm\Omega$. Resonance with external terahertz radiation occurs when $\omega_{THz} = \pm\Omega$.

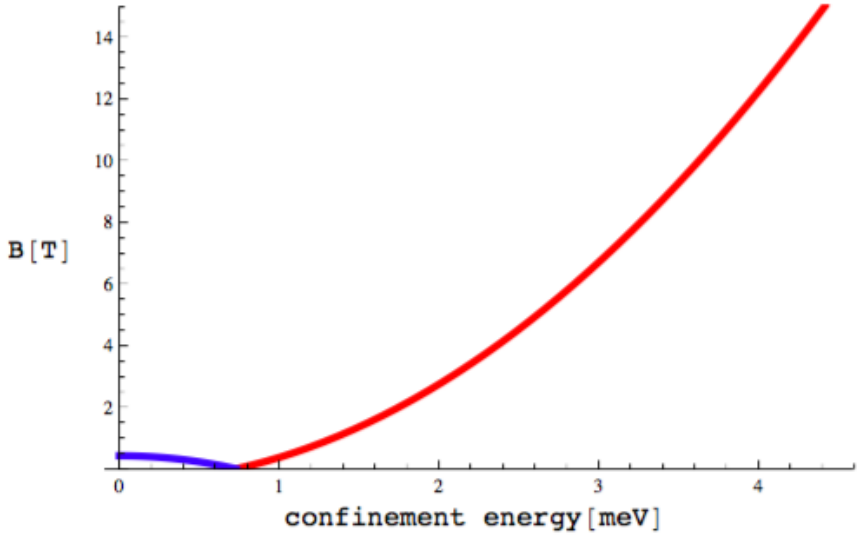

Figure 3.5: Resonance conditions, with two types of dipole transitions in the F-D spectrum. The magnetic field as a function of the dot confinement energy, where resonance between these transitions and the applied terahertz radiation occurs, $\omega_{THz} = \Omega+$ (blue) and $\omega_{THz} = \Omega-$ (red). $\omega_{THz} = 2\pi \times 177GHz$ [100].

Figure 3.5 is the theoretical calculation for the required magnetic field, in order to have resonance as a function of the dot's confinement energy. With the exception of zero field, all $\pm\Omega$ values are different from each other, meaning only one type of transition can be resonant with a particular monochromatic illumination. Only one type of transition is resonant at varying confinement energies. This is $\Omega+$ (blue) at low confinement energies and $\Omega-$ (red) at high confinement energies. If the confinement energy is too high, a field

of **B** >15T is required to get resonance.

This suggests that with frequencies of $\omega_{THz} = 2\pi \times 177GHz$, where 177 GHz is the frequency of the Gunn diode being considered as the source, a weakly confined dot is preferable as it would require lower fields for resonance.

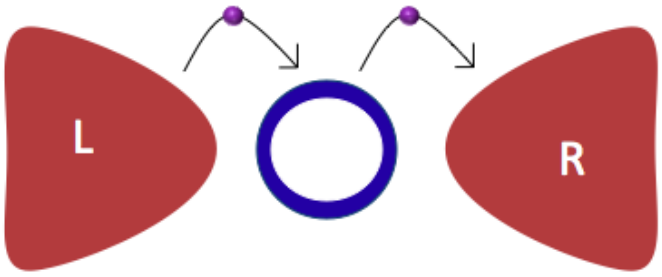

Figure 3.6: QD connected to the leads, labelled as **L** and **R**, with bias applied across the device.

We analyse the QD presented in figure 3.6 connected to the leads, labelled **L** and **R**, with bias applied across it. The "rate equation" can describe electron transport, as well as photon and phonon induced transitions. We can consider the many possible transitions by making some initial assumptions.

We assume the QD being weakly coupled to the **L** and **R**, and it is occupied by one electron in a regime of strong Columb blockade. We also consider weak electron-phonon coupling at low temperatures. Lastly, we take an incoherent terahertz source such that transitions between states are described by rates. This is different to coherent driving, such as e.g laser driving of an atom in resonance fluorescence [101]

The QD states we will need to consider are $\mid vac>$, representing the empty QD, and the set $\{\mid n_+, n_- \mid\}$, the single electron states with occupancy in the F-D orbital, where $n_\pm = 0, 1, 2...$, with the QD density matrix marked as ρ.

For our purposes of using the rate equation, only the matrix's diagonal elements are of interest, producing the master equation in the Lindblad form for the system as:

$$\dot{\rho} = \ell_{tunnel}[\rho] + \ell_{phonon}[\rho] + \ell_{THz}[\rho] \tag{3.6}$$

we can describe possible transitions of the system in terms of the standard Lindblad dissipator (superoperator), for some operator $\jmath$:

$$\mathcal{D}(\jmath)[\rho] = \jmath\rho\jmath^\dagger - \frac{1}{2}\{\jmath^\dagger\jmath, \rho\} \tag{3.7}$$

Following this we can take a look at electrons tunnelling in and out of the QD, described by the equation:

$$\ell_{tunnel}[\rho] = \sum_{n_+n_-} \Gamma^{in}_{n_+n_-}\mathcal{D}(\jmath^\dagger_{n_+n_-})[\rho] + \Gamma^{out}_{n_+n_-}D(\jmath_{n_+n_-})[\rho] \tag{3.8}$$

where the single electron jump operator is $\jmath_{n_+n_-} = |vac >< n_+, n_-|$. The incoming and outgoing decay rates have contributions from both **L** and **R** leads, where:

$$\Gamma^{in}_{n_+n_-} = \Gamma^L_{n_+n_-}f^+_L(E_{n_+n_-}) + \Gamma^R_{n_+n_-}f^+_R(E_{n_+n_-}) \tag{3.9}$$

$$\Gamma^{out}_{n_+n_-} = \Gamma^L_{n_+n_-}f^-_L(E_{n_+n_-}) + \Gamma^R_{n_+n_-}f^-_R(E_{n_+n_-}) \tag{3.10}$$

With Fermi functions described by $f^+_\alpha(E) = \frac{1}{1+e^{\beta(E-\mu_\alpha)}}$ and $f^-_\alpha(E) = 1 - f^+_\alpha(E)$ $(\alpha = L, R)$.

From this, the translations from quantum number $n_\pm$ to principal and angular momentum operators are,

$$n = \min(n_+, n_-) \qquad\qquad \mathcal{L} = n_- - n_+ \tag{3.11}$$

Where $(n, \mathcal{L})$ are often used. However (n_+, n_-) are much easier to work with and so they will be utilised in the following work. Based on equation 3.8 the position operator is,

$$\boldsymbol{r} = \frac{l\Omega}{\sqrt{2}}\{(a_+ + a^\dagger_-)\boldsymbol{e_+} + (a_- + a^\dagger_+)\boldsymbol{e_-}\} \tag{3.12}$$

Where $l_\Omega = \sqrt{\frac{\hbar}{m^*_e\Omega}}$ is the characteristic size of the F-D orbital, and $e_\pm = \frac{1}{\sqrt{2}}(e_x \pm ie_y)$ are the circular unit vectors. Following this, radiative dipole transitions can happen between states that are varying by one in either n_+ or n_-. The value of the dipole operator for these transitions are:

$$\boldsymbol{d_{n_+}}, n_+ + 1 =< n_+, n_- \mid e\boldsymbol{r} \mid n_+ + 1, n_- >= \frac{el\Omega}{\sqrt{2}}\sqrt{n_+ + 1e_+} \tag{3.13}$$

$$\boldsymbol{d_{n_-}}, n_- + 1 =< n_+, n_- \mid e\boldsymbol{r} \mid n_+, n_- + 1 >= \frac{el\Omega}{\sqrt{2}}\sqrt{n_- + 1 e_-} \tag{3.14}$$

with both types of transition having different frequencies, $\omega_\pm$, leading to radiation emissions of opposite circular polarisation. From this we have the standard expression of the radiative spontaneous emission rates in a vacuum [102],

$$\Gamma = \frac{1}{4\pi\mathcal{E}_\prime}\frac{4}{3}\frac{\omega^3 d^2}{\hbar c^3} \tag{3.15}$$

If we introduce this expression into a medium, $\mathcal{E}_\prime$ is replaced by $\mathcal{E}_\prime\mathcal{E}_r \approx n^2\mathcal{E}_\prime$ and c is replaced by $\frac{c}{n}$, where n is the refractive index. This means,

$$\Gamma_{n_\pm, n_\pm+1} = \frac{4n\alpha\Omega_\pm^3}{3c^2}\frac{l_\Omega(n_\pm + 1)}{2} = \frac{2n\alpha(n_\pm + 1)}{3c^2}(\Omega_\pm^3 l_\Omega) \tag{3.16}$$

and the field dependence is introduced by Ω and l_Ω. The decay rate is shown in figure 3.7. In this figure the Ω_- rate decreases strongly with field, as the frequency of this transition tends to zero. Ω_+ however tends towards the bulk Landau level splitting, $\omega_c \sim B$, and the rate increases as B^2. A less confined dot produces weaker transitions.

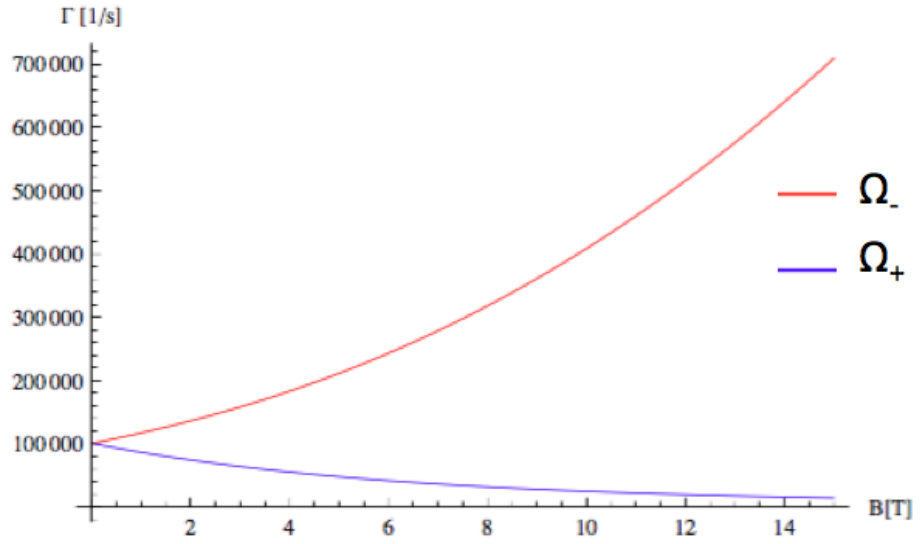

Figure 3.7: Decay rate for transitions in the F-D spectrum, corresponding to $n_\pm$= 0 in equation 3.16. This is done assuming L_{conf} = 10 nm, giving $\hbar\omega_0$ ≈11.4 meV as well as $m_e^* = 0.067m_e$ and $n = \sqrt{13} \approx 3.6$ [100].

The dominant relaxation mechanism for lateral QD's tend to be due to couplings to acoustic phonons [103, 104]. Using [105], the relaxation rates due to LADP (electron-

acoustic phonon interaction due to the deformation potential) and LAPZ (electron-acoustic phonon interaction due to the piezoelecric field for longitudinal modes) can be calculated and displayed [100]. The calculation for this system matches that of [105] perfectly. TAPZ, shown in figure 3.8, is the electron-acoustic phonon interaction due to the piezoelectric field for the transverse modes [106].

The three phonon processes contribute to the phonon-induced relaxations, with rates of orders 1-10 ns^{-1}, specially at finite B-fields.This is a longer time compared to the relaxation time for radiative rates. The equation in reference [105] also describes regions where electron and phonon wave functions are approximately opposite in phase, leading to suppression of phonon relaxation rates.

For this to happen, $L_z \approx j\lambda_q$, where L_z is the confinement length in the growth direction, λ_q is the phonon wavelength and j is an integer. The phonon wavelength, which is of course related its frequency, is therefore determined by which transition frequency we have, ω_+ or $\omega-$. The anti-phase condition can be re-written in energy units as,

$$(\hbar\omega_\pm)^2 \approx 16\pi j E_z T \tag{3.17}$$

where $E_z = \frac{\hbar^2\pi^2}{2m_e^* L_z^2}$ refers to the z direction confinement energy, if we assume a square well. $T = \frac{1}{2}m_e^* c_\sigma^2$ is the electron kinetic energy whilst it travels at the speed of propagation of phonons, with polarisation σ.

Seeing how ω_- always decreases with field, observing this suppression in ω_- requires $(\hbar\omega_0)^2 \geq 16\pi E_z T$. ω_+ increases with field, and $j > 0$ is arbitrary, there is always some j such that suppression occurs. It should be noted that following suppression of LA phonons, the TA phonons will not be anti-phased since $c_{TA} \neq c_{LA}$.

Figure 3.8 is the calculated approximate rates for both $\omega_\pm$ transitions for parameters where equation 3.17 holds. It can be observed that there are sharp dips in phonon rates for both transition frequencies.

Following this line of thought, whether or not photon emission can be observed is dependent on the relative strength of radiative and non-radiative transitions, quantified by the quantum efficiency Q,

$$Q = \frac{\Gamma_{rad}}{\Gamma_{rad} + \Gamma_{non-rad}} \tag{3.18}$$

with Γ_{rad} and $\Gamma_{non-rad}$ referring to decay rates of radiative and non-radiative tran-

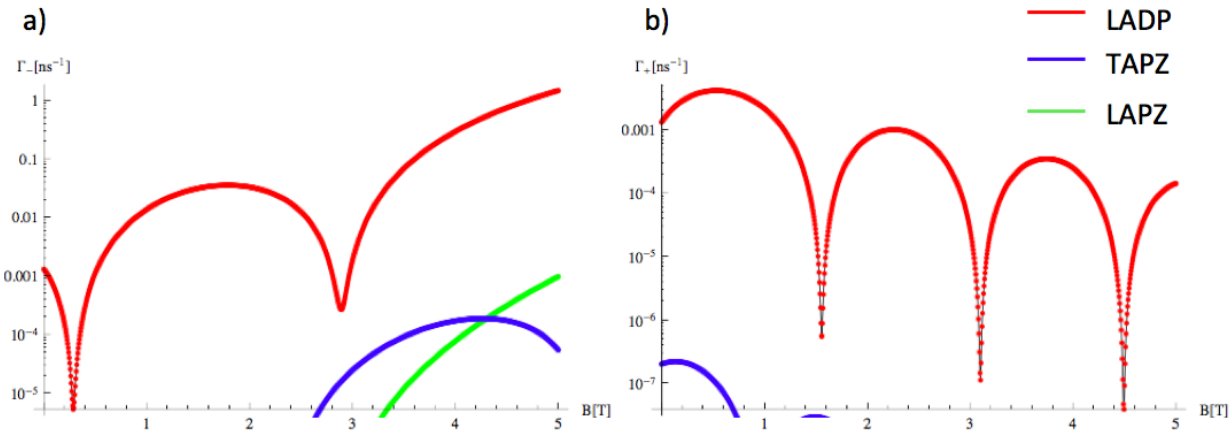

Figure 3.8: Relaxation rates for a) ω_- and b) ω_+ transitions due to phonon scattering. It can be observed that both rates suffer suppression from phonon-electron anti-phase [100]. It is assumed that $\hbar\omega_0 = 5$meV and $L_z = 10$nm. Other parameters are set similarly to [105].

sitions respectively. In figure 3.9, we see calculations of Q for values of $\omega_\pm$ given in figure 3.8 [100].

In the regions of phonon suppression, $Q \approx 1$. Meaning transitions are photon emitting.

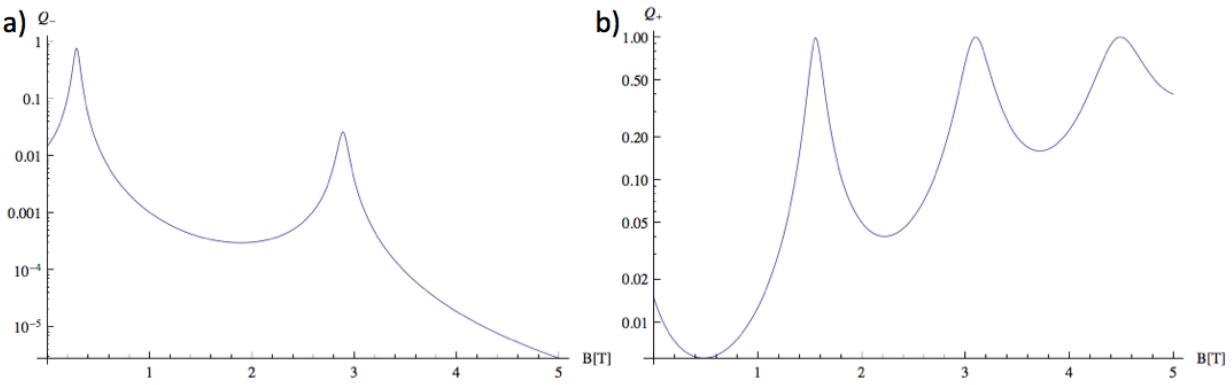

Figure 3.9: Calculated Quantum efficiency for a) ω_- and b) ω_+ rates in figure 3.8. An ideal emitter would have $Q = 1$ [100].

3.3 Experimental set-up

This section discusses the experimental set-up for studying the electron pump.

The 2DEG formed in the GaAs/AlGaAs heterostructure can be depleted by applying negative bias to two metallic gates on the substrate surface, right above the etched channel. These two gates are positioned within close proximity of one another, with about a 50 nm gap between the two and a circular design in the centre were electrons are trapped between the potential wells in the quantum dot (QD).

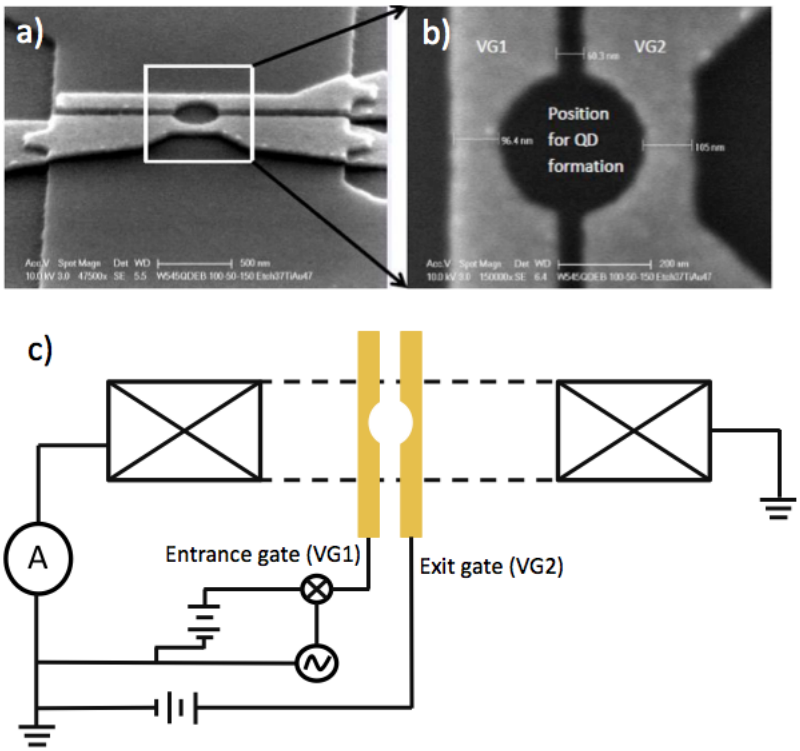

Figure 3.10: a)SEM image of the electron pump, consisting of two metallic gates (VG_1 and VG_2) deposited on an etched 2DEG channel, capable of creating a QD when negative bias is applied. b) Close up of the area where the QD is formed with the gate and gap parameters. c) Basic schematic of the electron pump set-up and connections. The 2DEG is formed 70nm below the surface, with two Ti/Au gates deposited on the substrate. The entrance gate VG_1 has DC and AC voltage (V_{rf}) applied, and the exit gate (VG_2) only has DC voltage applied to it, together creating a dynamic QD [107].

Two metallic gates denoted as VG_1 and VG_2, correspond to the entrance and exit gates respectively are shown in figure 3.10. When biased, they form two potential barriers, with a quantum dot (QD) in the center between the barriers. A mix of AC and DC bias is applied to the entrance gate (VG_1), whilst DC bias is applied to VG_2.

Because of the small size of the electron pump, there is a real danger of the pumps gates blowing due to electrostatic discharge, so its very important that the set-up is well grounded. Care is taken to ensure everything is connected to a scientific ground. The scheme of the experimental set-up is shown in figure 3.11.

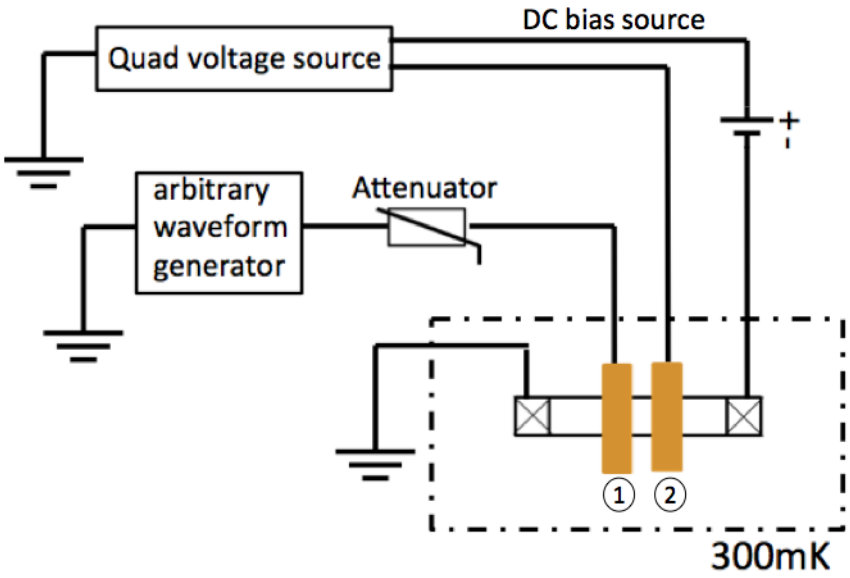

Figure 3.11: Schematic of the electron pump, with the entrance gate and exit gate labelled as 1 and 2 respectively.

Prior to measurement, the sample is cleaved from a greater batch, the protective polymer is cleaned away with acetone and isopropanol. It is mounted onto the sample holder with GE vanish and bounded with gold wires.

Photographs of the sample are shown in figure 3.12. In order to study the pump map quantisations with the highest possible accuracy, we use a dry refrigerator with a magnetic field. This is a system with the capability of going down to 3 mK and apply up to 14 Tesla of magnetic field. This system was used for both studies presented in section 3.4.

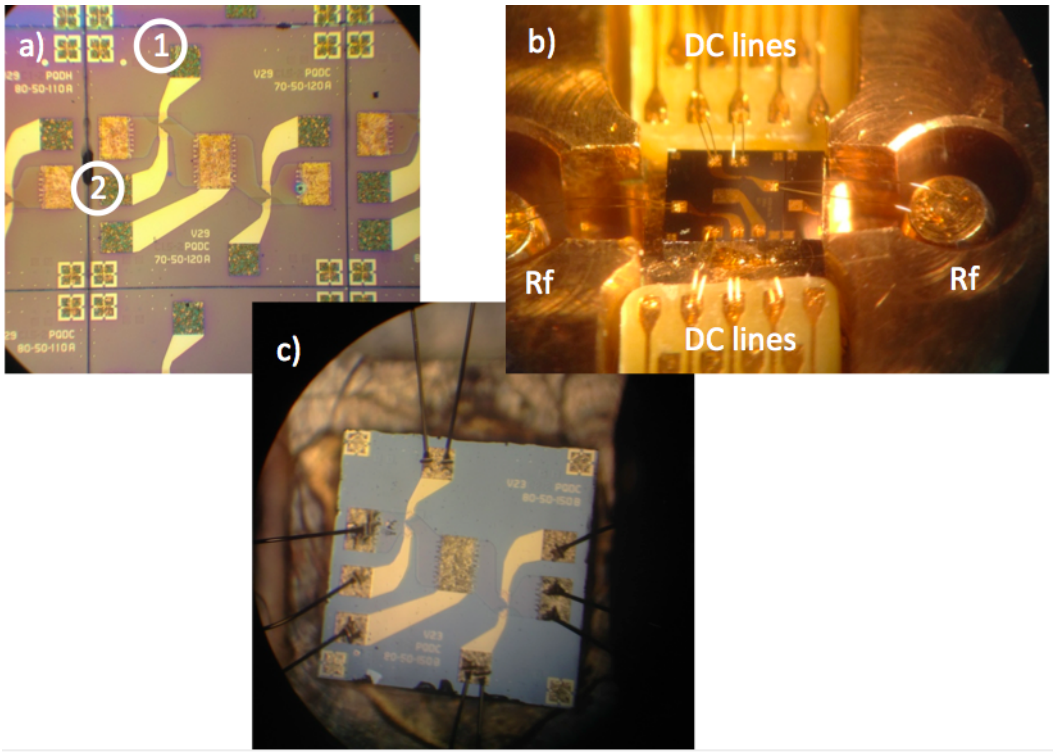

Figure 3.12: a) Batch of samples prior to cleaving. Each sample has two electron pump devices, which share a common ohmic contact. Numbers 1 and 2 refer to entrance and exit gates of one device respectively. b) Sample has been attached to the sample holder using GE vanish and bonded to the DC pads and RF pins as necessary. c) A closer look at the device after bonding.

3.4 Experimental analysis

3.4.1 Characterisation of e-pumps

As discussed in section 3.2, an electron pump is in essence a dynamic quantum dot with a predictable throughput of electrons. However, our dot's elevation above the Fermi energy sets it apart from other quantum dots, e.g mesoscopic capacitors [108]. The quantisation of the output current through this device has been the subject of a number of papers [109–111]. This may ultimately play a part in completing the metrological triangle, re-standardising the ampere [10].

In order for an electron pump to be judged "usable", it must pass the characterisation test: it should produce quantised current within suitable parameters. The quantised current is $I = nef$, where n denotes the number of electrons passing through the dot, e is the electron charge and f is the frequency applied to the entrance barrier (VG_3). The current passing through the dot can be controlled as a function of ef multiples, as the formula suggests.

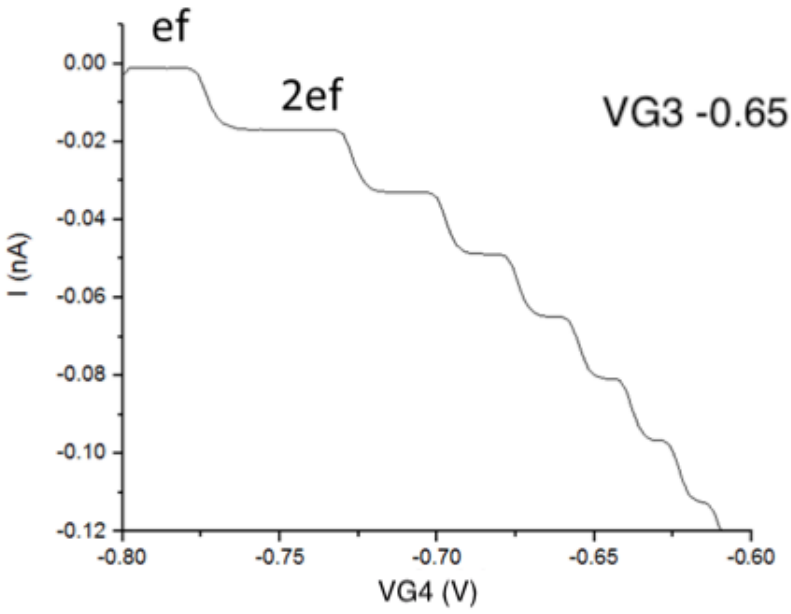

Figure 3.13: Current pumped through. The entrance gate is set to -0.65 V (VG_3). 100MHz is applied to the entrance barrier.

Figure 3.13 shows the pumped current as a function of the entrance gate DC voltage, with the exit gate voltage set to -0.65 V. The current pumped through the dot is quantized by ef . Figure 3.14 is a compilation of individual current traces in varying exit and

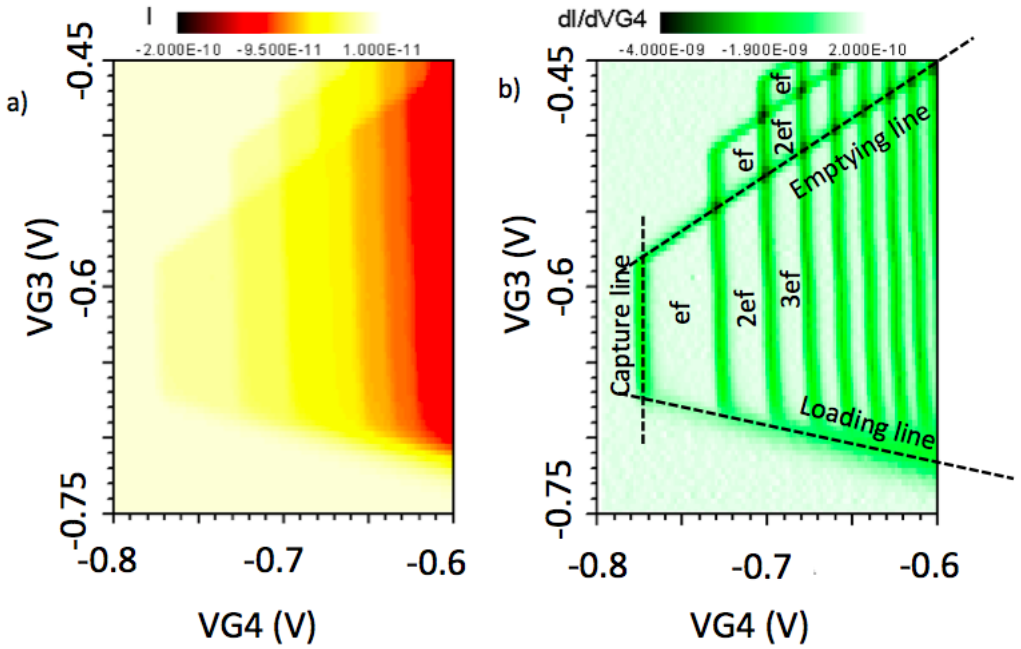

Figure 3.14: a)Current as a function of entrance gate VG_3 and exit gate VG_4 at 100MHz b) The derivative QD current.

entrance gate voltages.

In figure 3.14b, the capture line corresponds to the point with both barriers have similar height i.e. equal probability of the electron tunnelling to either source or drain. The loading and emptying lines refer to the entrance barrier being either lower or higher than the exit barrier respectively, allowing in the first instance for the electron in the dot to back tunnel to the source and in the second instance encouraging the electrons to forward tunnel into the drain, as shown in the master equation referred to in section 3.2.1.

Along the emptying line, when electrons are forward tunnelling to the drain, there are certain entrance barrier heights where only a limited number of electrons are allowed to flow to the drain. An example of this can be seen as *ef* current continuing out of a *2ef* line in figure 3.14b. Beyond this line, a stable QD cannot form with greater than $n-1$ electrons. This is a key part of the "Decay Cascade model", and is a reason for the dot needing to load more electrons than it will eventually pump [98].

This electron pump is considered "usable" for the intended application, as the electron pump shows no unexpected features that may introduce unexpected anomalies into the measurements.

3.4.2 Excitation states in e-pumps

As previously discussed, we would like to use the electron pump as a terahertz photon detector and emitter. In this section we focus on the possible emitter capabilities of the electron pump. It was discussed earlier in chapter 3 that a quantum dot can be referred to as an artificial atom, due to its similarities in the way the electron in the dot occupy energy levels. This means that if an electron with extra energy was to enter the dot, it would most likely occupy an excited level above the ground state (if we assume an empty ground state in this instance). Once the electron relaxes to the ground state, it releases the excess energy in the form of a single photon, with the photon energy corresponding to the energy level separation in the dot.

Up to this point all measurements have been performed without applied magnetic field. Resolving these excitation states without a magnetic field, although possible for small dots, is quite difficult due to zero separation of states. Applying a magnetic field (B-field) leads to quantisation of energy states in the dot which are much more visible.

I

Increasing the B-field not only increases the energy level separation in the dot, but it also leads to flatter plateaus, figure 3.13. Therefore the steps are more clearly defined now that there is further lateral confinement in the dot. This increases the accuracy of the quantised current pumped through the dot, which is of great interest for use in the restandardisation of the ampere.

By increasing the frequency applied to the entrance barrier, electrons load into the dot with excess kinetic energy. This means it is possible to load an electron into a higher energy state in the dot.

We can resolve a line appearing between the *ef* and *2ef* spacings in the pump maps, figure 3.15, reflecting the loading of electrons into the excited state of the QD. Data in figure 3.15 was taken at 4T and frequency of 500MHz. Electrons are excited non-adiabatically, and so to enter the excitation energy levels in the QD, as previously suggested by Kataoka et al. in 2011 [99].

However, in contrast with Kataoka's presented data in [99], the current in the excitation state plateau extends beyond the *1ef* plateau. This is the first such observation and It is a feature of this specific electron pump's ohmic contacts. It suggests that electrons having been loaded into the excited state, are leaving the QD without relaxing to the ground state. Physically this could mean that having moved to higher energy states,

the electrons are tunelling out of the QD exit barrier more easily prior to the intended pumping out of the electron to the drain. This is undesirable as there is little chance of a photon emission as the electron is likely to leave before releasing its excess energy.

In order to allow the electron to relax to the ground state, it was necessary to identify a way of encouraging the electron to remain in the dot long enough to emit excess energy. An Arbitrary Waveform Generator (AWG) was used to apply a waveform to the entrance barrier in order to introduce more control over the electron movement.

The AWG generates a waveform, applied to the entrance barrier. During the measurements shown in figure 3.16, a basic sine wave was applied. In order to encourage the excited electrons in the QD to remain long enough to relax to the ground state, a sine wave with a flat region was introduced, corresponding to the point at which the excited electrons were still within the QD [112], figure 3.16. A direct comparison between a simple sine wave and a sine wave with a flat shows excitation current plateaus extending pass the *ef* line vanish after the flat is introduced.

A pertinent matter to investigate is the energy value of the excitation lines. This identifies whether any excess energy released would indeed result in photons in the terahertz range. As the bias applied to the gates cannot be converted directly to energy, there is a need to be more inventive in order to derive this information.

Firstly one determines the frequency at which it is possible to detect the first excitation energy level on the pump map. An entrance barrier value is selected, at which the first plateau and excitation level are both clearly visible, and the exit barrier voltage is swept whilst stepping the magnetic field. By attempting to fit the Fock-Darwin spectrum to the first excitation state, an energy value may be derived. Figure 3.17 shows a pump map taken for the electron pump in question.

The large white feature appearing to dominate the pump map is the rectifying current. This is the current that is flowing out of the QD against the designated flow of current in the system, going towards the source rather than the drain. It is a feature of this specific electron pumps ohmic contacts and could not be removed by varying any parameters, only suppressed.

Figure 3.18 shows the data from figure 3.17 re-plotted, with the Fock-Darwin spectrum fitted to the first excitation line. As can be seen in this particular case, the energy given is around 5meV. This corresponds to 1.2THz, confirming that should the device successfully emit photons as expected, the device would indeed be a source of terahertz

radiation.

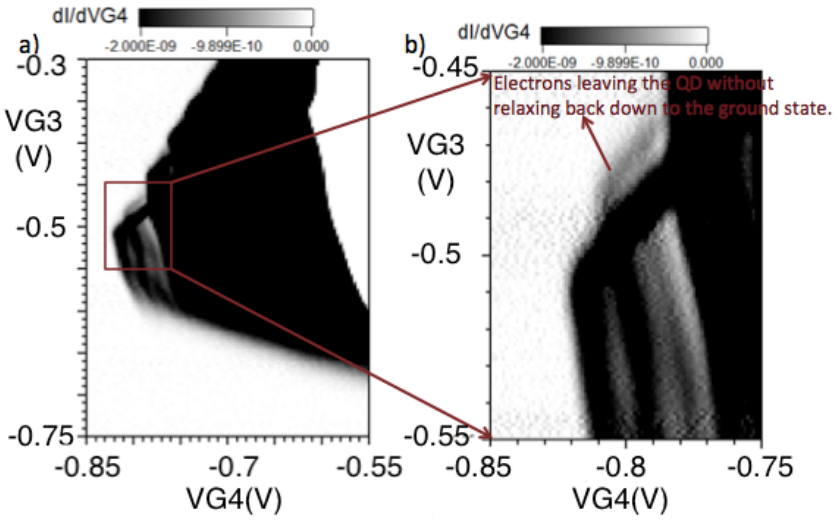

Figure 3.15: a) Derivative current. The excited electrons are leaving the QD without relaxing back down, b) close up of our region of interest.

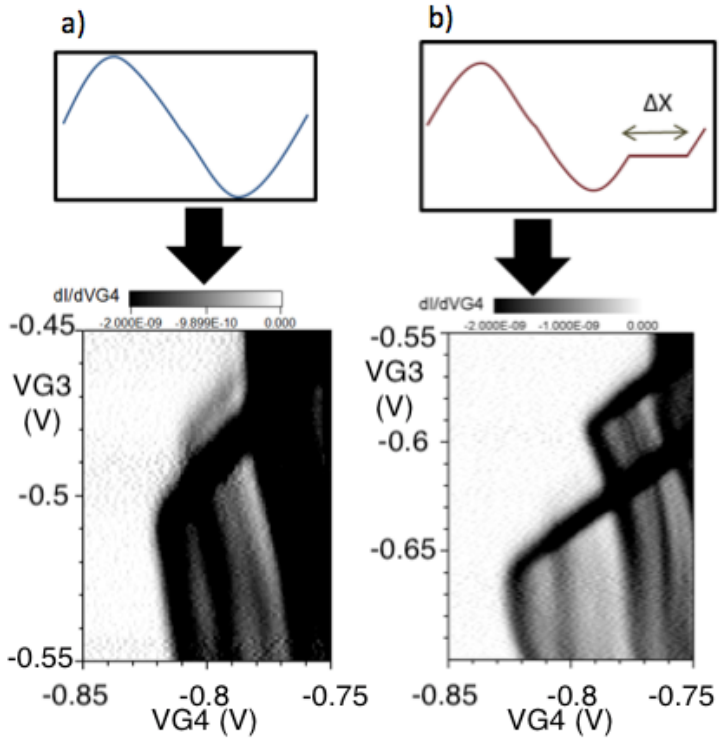

Figure 3.16: a) Data from figure 3.15 with a normal sine wave applied along with 500MHz frequency at 4 Tesla. The excited electrons are still leaving the QD without relaxing back down b) Same e-pump, after a flat is introduced. The excited electrons are no longer leaving the dot. The data is taken at 300MHz and 4 Tesla.

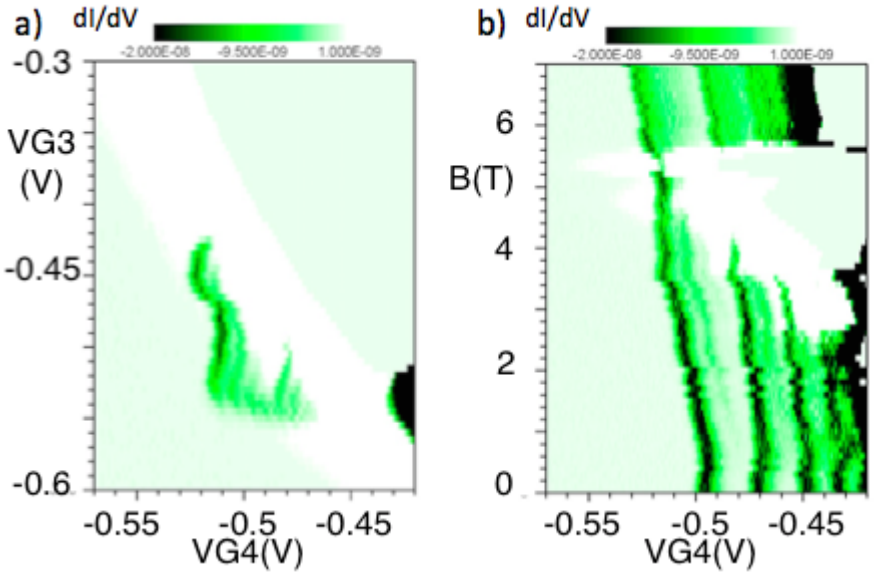

Figure 3.17: a)Pump map at 1GHz and 4 Tesla, including rectifying current, which can be seen as a white feature almost drowning out the pump map b) Stepping the applied magnetic field, from 0T to 7T at -0.52V for VG3. The rectifying current makes its appearance once again as a white feature drowning out some of the data.

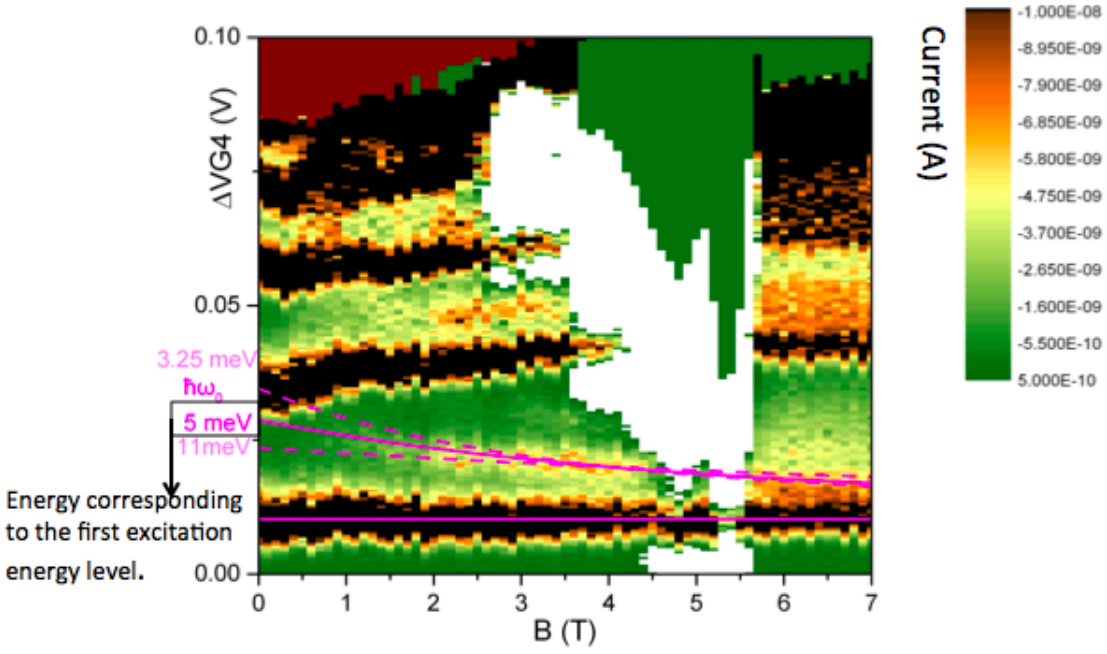

Figure 3.18: Refitting figure 3.17b at 1GHz with VG_3 kept at -0.51V. The straight pink line shows $L1$, the solid curved pink line indicates the most likely position of the first excited state at this frequency, whilst the dashed lines pin-point the other lower probability routes for the excited levels.

3.5 Summary

This chapter has served as an introduction to the electron pump. We discuss the devices fabrication and fundamentals of its operation. We also looked at electron quantisation using the electron pump, and the possibility of electrons loading into higher energy states within the dot when loaded with excess kinetic energy. The value for the lowest excited state was measured to be 5meV for the device in question. This corresponds to a photon with 1.2THz of frequency.

Chapter 4

Electron pump - QPC device for dot occupancy detection

The quantum point contact (QPC) coupled electron pump is an alternative version of the electron pump discussed in chapter 4. In this electron pump both gates have DC bias applied. In this case, the dwell time of the electron in the dynamic quantum dot can be probed by the QPC outside the electron pump's exit gate. The QPC gate is defined between the ohmic contacts numbered 2 and 3 in figure 4.1. This gate can pinch the current between ohmics contacts 2 and 3,since this channel is capacitively coupled to the electron pump, it is able to sense the change in charge of the electron pump. An addition of extra electrons to the dot results in a further restriction of current flow through the channel [109]. This system may have the potential to act as a terahertz detector. The energy level separation in the dot due to spacial quantization corresponds to energy in the terahertz range. There is a possibility that one may detect terahertz radiation by monitoring the electron dwell time in the dot under applied radiation.

The fabrication of this device follows all the steps of a standard electron pump with the addition of an extra gate and ohmic contact, the details can be found in section 3.1 of chapter 3.

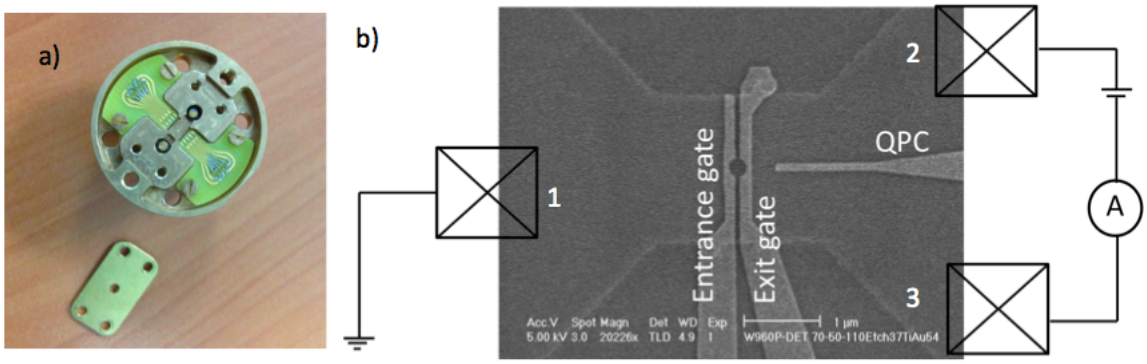

Figure 4.1: a) Basic design of the electron pump sample holder, including 18 DC lines and 2 RF lines. Each substrate contains 2 devices wired to the sample holder. b) SEM image of electron pump/QPC device, with the basic device schematic design and ohmic contacts attached.

4.1 QPC coupled electron pumps

In order to detect the electron occupancy within the dot, the QPC coupled electron pump is operated slightly different to the standard pump discussed in chapter 3. As shown in figure 4.2, the entrance barrier dips below the Fermi energy (the value of which is referred to as the loading voltage) and rises back up to the same height as the exit barrier (the reading voltage) trapping the electrons. The barriers are kept at the final chosen height until it is registered that the electron has left the dot. This is the cycle used to study electron relaxation. The QPC coupled electron pump discussed here has been used before also for detection of the errors in the electron pump capture process [109].

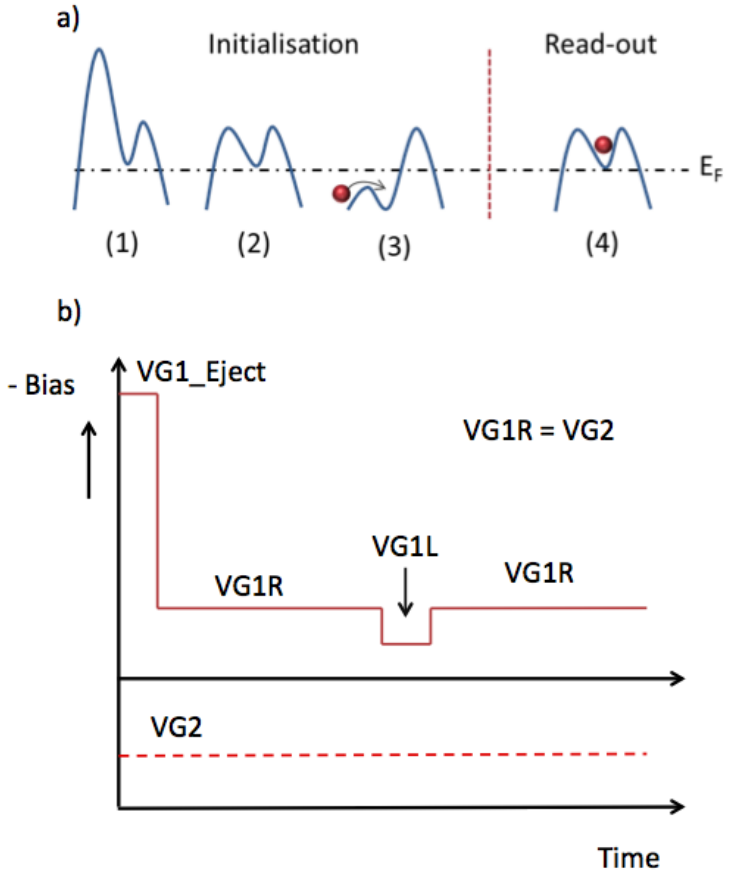

Figure 4.2: a) The device operation cycle, showing the entrance barrier rise (1) in order to eject electrons from the dot, then dipping below the Fermi level (3) and loading an electron into the dot. In (4) both entrance and exit barrier height are equalised and held still.. The run continues until the electron(s) leave the dot, at which point the run is terminated and the time recorded. b) events of the cycle in terms of entrance and exit barrier voltages, where VG1 is the voltage at the entrance gate and VG2 is the voltage at the exit gate respectively.

4.2 Experimental set-up

In the electron relaxation experiment, the pump is not operated dynamically, but simply as a regular quantum dot once loaded. The use of QPC gates to measure dwell time is not unique, and has been performed by others, with an accuracy of 10ms and 4μs respectively [113, 114]. However we are the first to apply it to this particular design of the electron pump, and using a HP3458A Femto digital multimeter allowed us to have an accuracy of 2ms. To achieve this, the multimeter is triggered during the measurements so that all displays and other unnecessary functions are abandoned, for it to achieve the precision required. At the end of the measurement the Femto are reset to low speed mode.

The experimental schematic can be seen in figure 4.3.

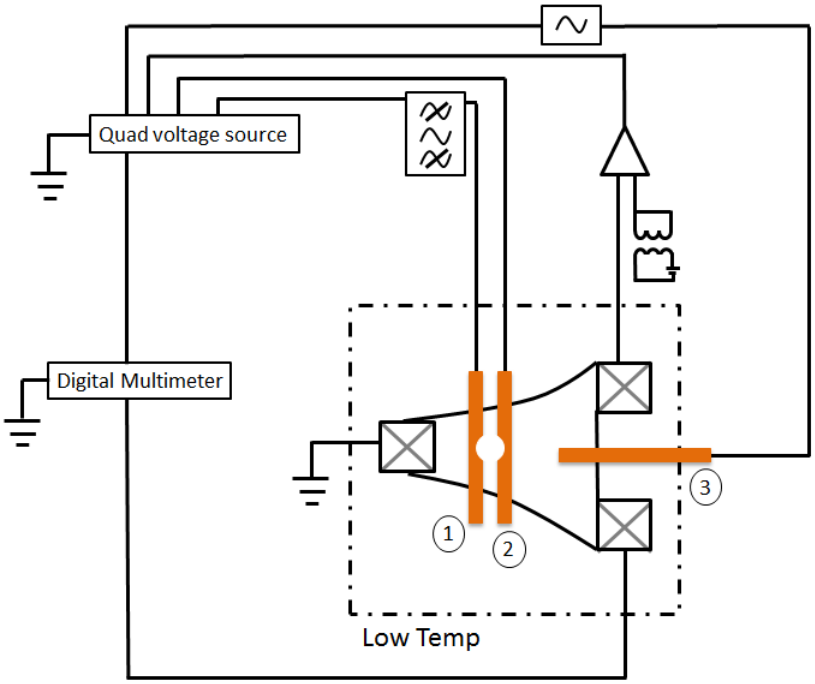

Figure 4.3: A simple schematic of the experimental set-up used in order to study electron dwell time in the electron pump using a QPC gate (marked as 3). In this arrangement the pump is not operated as a dynamic quantum dot as it usually is, as seen in the previous section. The entrance gate (marked as 1) is driven by DC voltage, similar to the exit barrier (marked 2).

The cryostat was a Heliox model 3He refrigerator, with a base temperature of 300mK and up to 14T of applied magnetic field.

Since this experiment was designed to study the application of the electron pump as a terahertz detector, a terahetz wave-guide was incorporated into the set-up. This was

to allow photons from a terahertz source at room temperature to reach the device at low temperature.

The probe, designed for the Heliox dry refrigerator, included the 2.5 meter terahertz wave-guide. A small opening into the sample holder exposes the device to the wave-guide. The wave-guide size standard is recorded as WG 28 (this being a RCSC standard wave-guide sizing, with WG28 having parameters of 2.032mm by 1.016mm), and it tappers at the end to connect to the sample holder. A number of tests have been carried out to ensure the radiation is passing through the wave-guide, ensuring the attenuation introduced by the length of the wave-guide is not hindering the transport of photons down the probe. It was confirmed that the radiation from the source was transported through the probe despite the heavy attenuation, although the exact power could not be recorded with the available detectors at the time.

Incorporating this wave-guide introduced some difficulties. As seen in figure 4.3, the wave-guide was placed in the centre of the cryostat probe, connecting the source at room temperature to the device at low temperature. This made fitting all the wiring inside the probe fairly challenging. The true difficulty arose when the refrigerator/cryostat failed to cool down below 4K temperature. We originally concluded that this could be due to the wave-guide sinking heat into the 3He pot from room temperature.

After a few cooling attempts we determined that the failure was the outcome of a combination of factors. Unsuitable RF cable material, combined with the waveguide's tendency to lean to one side in the probe and thermally couple the sorb and 1K pot seemed to be the cause of the failure to cool down. Once these problems were dealt with, the device was successfully measured at base temperature, with the fridge able to remain at low temperature initially for 20 hours and on the second round of experiments, for 15 hours.

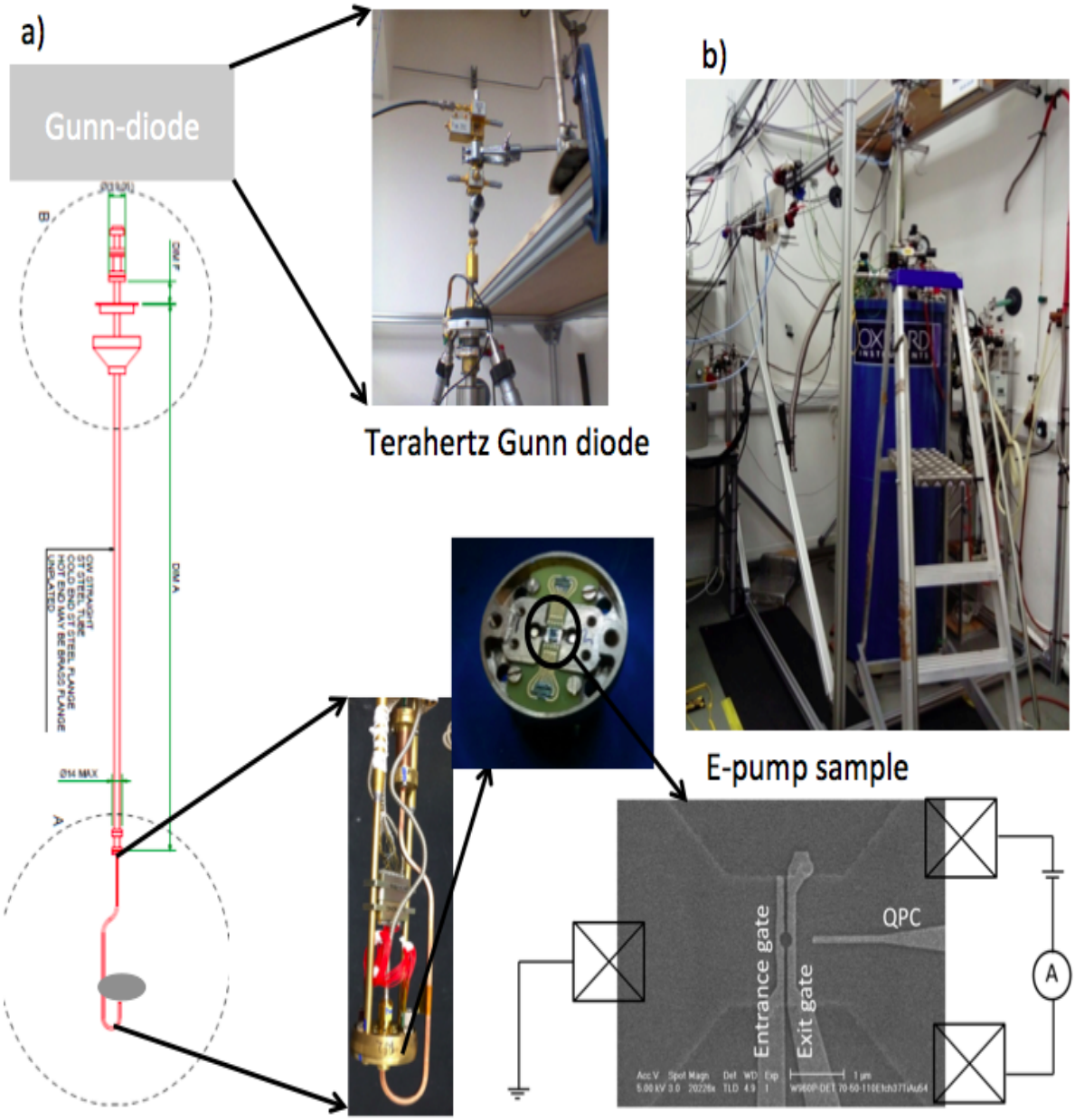

Figure 4.4: a)The 3He Heliox probe, designed to include a 2.5 meter terahertz wave-guide. This wave-guide starts from room temperature, were it is connected to a Gunn diode to low temperature, were it terminates after reaching the sample holder. The Gunn diode has frequency of 177GHz. Probe designed By J. D. Fletcher, device designed by S. Giblin. b) The 3He Heliox system.

It is known that these devices are susceptible to electro-static discharge (ESD) than bigger devices. A small sudden influx of electrons is enough to blow up the channels, or damage gates in disastrous irreparable ways. In order to avoid this, certain precautionary steps were taken. It is of great importance to have the measurement system grounded to avoid instances of ESD spiking. Any attempt to engage with the measurement set-up should only take place when individuals are also connected to the ground, avoiding any ground loops in the system.

Since our device operates at low temperature, the Heliox needs to be fully grounded prior to starting the experiment. The diagram shown figure 4.5 demonstrates how the system was safely grounded, and schematics for the experiment in question can be seen in figure 5.1a, although the same principle is carried out for all electron pump experiments.

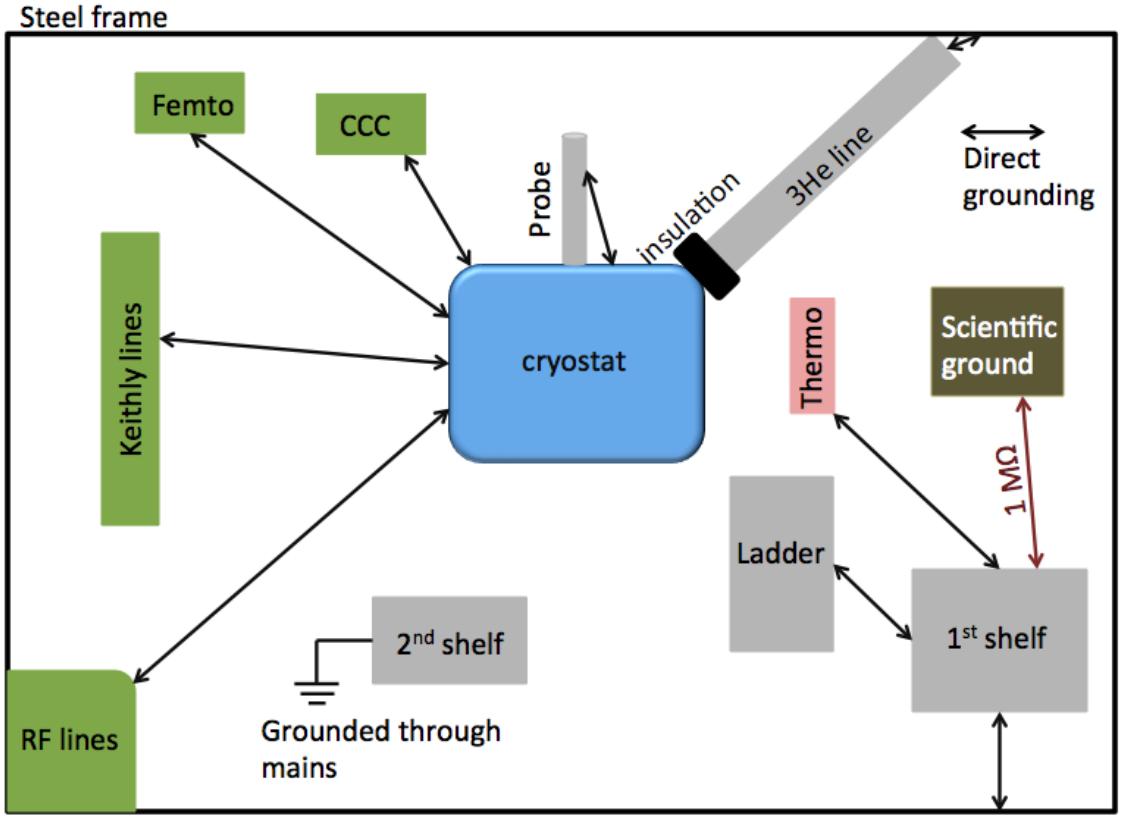

Figure 4.5: The grounding of electronic and conductive surfaces and devices in order to avoid compromising the device through ESD.

4.3 Analysis - electron relaxation rates in electron pumps

Having determined in section 3.4.2 that the energy gap between the ground and excited state does indeed correspond to radiation in the terahertz range, the next step is to look into the possibility of using the electron pump as a terahertz detector. One would need to study the dwell time of the electron in the dot in the absence of terahertz radiation i.e. when the electron is occupying the ground state, in order to eventually perform the ideal final version of the experiment. This ideal experiment will study and compare the electron dwell time in the dynamic quantum dot with and without applied radiation. At that point, should the electron absorb the terahertz radiation it may have enough energy to move from the ground state to first excited state, which in turn would reduce its dwell time in dot as it is easier for the electron to tunnel out of the dot from a higher energy level.

Currently we are focusing on measuring the electron dwell time in the dot in the absence of radiation. We study the dwell time of an electron loaded into the QD by observing the current passing through the contacts outside the exit barrier, figure 4.1 (the QPC gate and exit gate). We study the natural decay time of the electron out of the quantum dot without any external encouragement. It is important to note that at this point we are using the electron pump as a quantum dot rather than a dynamic quantum dot. Once the electron has been loaded into the dot, both barrier potentials are set to stable values, and remain there until the electron has decayed out, or the measurement run has been terminated.

We plot a map, similar to figure 3.14, displaying the electron dwell times as a function of barrier heights, see figure 4.6. Here the dwell time at 3 Tesla is displayed, as a function of the exit barrier read voltage and the entrance barrier read voltage. The dwell times cannot be resolved below 2ms as that is the smallest step that we are able to resolve. Due to experimental time constraints, the measured dwell time has a cut off point of 1 second. Any longer dwell times are not recorded.

The dwell times displayed are taken as an average of 500 cycles in which the electron is loaded into the quantum dot and its decay time is measured.

The dwell time maps give information which corresponds to the pump map, whilst also providing the lifetime of the state. The dwell time is zero when one barrier is pushed far higher than another, allowing the electron to tunnel through to the source or drain

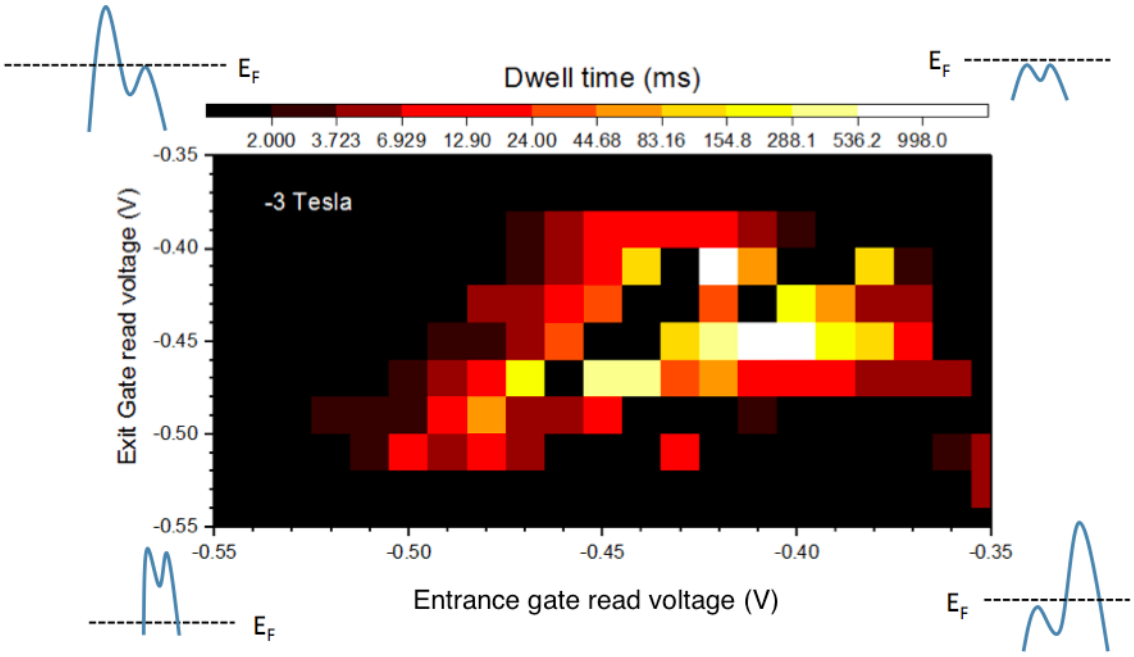

Figure 4.6: Dwell time map for the electron pump at 3 Tesla. Black denotes zero/low dwell time and white indicates the maximum dwell time we are able to record. At the far ends of the axis the dwell times are zero, as barrier positions either encourage forward/back tunnelling or both barriers are far above/below the Fermi level to contain any electrons in the dot.

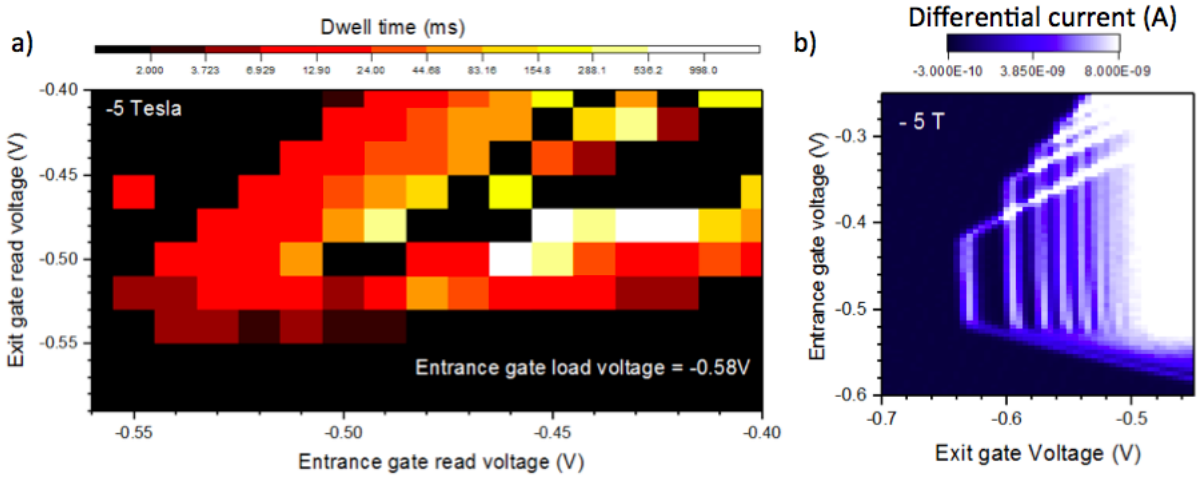

Figure 4.7: a) Dwell time map at 5 Tesla. The entrance gate loading voltage is set to -0.58V. b) The map for the same device showing the electron pump current at the same field.

over the lower barrier. There is also zero dwell time when both barriers are either far above or below the Fermi level. This corresponds to the lack of current outside emptying,

loading and capture lines shown in figure 3.14.

This is why in figure 4.7 the dwell time map and differential current map at 5 Tesla are shown side by side. For our purposes it is interesting to compare the electron dwell time as a function of entrance barrier height for a number of different magnetic fields.

We know that as the applied magnetic field is increased, the dot becomes more isolated from the source and drain. It is reasonable to consider the electron's maximum dwell time would be when the entrance and exit barriers have similar heights, and the tunnelling rate to both the source and drain are approximately the same. This can be seen in figure 4.6, where the entrance and exit barriers are set to -0.43V and -0.41V respectively. The Decay Cascade Model [98] discussed in section 3.2 of chapter 3 (equation 3.5), indicates the range in which the electron has its maximum dwell time increased as the magnetic field is increased (this is discussed in depth in the referenced paper). This should also hold true for the overall dwell time of the electron in the dot.

Figure 4.8 shows a typical experimental cycle as recorded by the Labview analysis software specifically written for this experiment. Once an electron is loaded into the dot, we wait until all the electrons inside the dot naturally decay out of the dot. The occupation of the dot affects the current through the channel between the QPC and the exit barrier by further restricting the passage of current through the channel. This can be seen in figure 6.9, as the current is reduced from 4.4nA to 3nA when 2 electrons are loaded, increased to 3.8nA when there is a single electron, and finally goes back to 4.4nA when all electrons have left the dot.

For each selected barrier height the procedure was repeated 500 times in order to obtain a meaningful statistic. The collective data is plotted in a histogram format and the dwell time is extracted from the data.

Figure 4.9 shows the extracted dwell times for various barrier heights and magnetic fields. This was the first iteration of the dwell time experiment. The data confirms some predictions based on work previously done by Fletcher's 2012 paper [110]. The dwell time increases as the magnetic field increases, and the electron can remain at its optimal position for a larger choice of barrier heights. This can also been seen in the map comparisons in figure 4.6 and 4.7, with data taken at 3 Tesla and 5 Tesla respectively.

Another prediction discussed in Fletchers paper [110] was the increased sensitivity of the electron to change in barrier height at higher fields. This can been seen more clearly when directly comparing data from 3T, 5T and 10T. We extracted decay rates

from the dwell times for these field values and compared the results directly to theoretical predications presented in the 2012 paper, see figure 4.9. It was not possible to obtain data at 0T because the dwell time was smaller than the resolution.

We see a more rapid decay rate at higher fields and an increased sensitivity to barrier change. This supports the idea that increasing the magnetic field increases the accuracy with which quantized current is pumped through the electron pump.

Before attempting this experiment once again in the presence of terahetz radiation, another iteration of the exact same experiment was performed with the same device 8 months after the initial tests, with the explicit aim to take data for more parameters for better comparison. The second round of data however, yielded some unexpected results.

Figure 4.10 shows another iteration of the same experiment, with smaller step sizes, performed with the device 8 months after initial tests, shown in figure 4.9. One can immediately see differences between the two data sets. In place of the clear change in dwell time, from a shallow slope at low fields to a sharper one at higher fields we end up with dwell times with unclear patterns and dips and peaks at odd locations.

This is in first glance, is not in agreement with our master equation. In order to explain the change in behaviour a number of possibilities were explored and investigated. After close inspection it came to light that at various magnetic fields above 4 Tesla, there were more cycles in which initially two electrons were loaded into the dot. This is in contrast to the first experiments were more often than not a single electron was loaded into the dot. What this means in a quantum mechanical perspective is a change in system once the first electron leaves and only one electron remains in the dot.

A closer look at how this translates to electron behaviour in shown in figure 4.11, for the data taken at -6 and -7 Tesla. It can be seen that once all but one of the electrons have left the dot, the decay of this final electron returns to an exponential decay since the fit appears as a straight line in the log plot. This was what was initially expected of the dwell time behaviour (remembering that the decay rate is $1/dwelltime$). This indicates that the number of electrons in the dot has played a part in the change of electron behaviour in the dot.

This behaviour could be explained if we go back to our discussion of modelling the dwell times using the rate equation in Chapter 3, section 3.2. In this section we discussed that the electron's behaviour can be described by this equation, and following that the single electron in the dot would have an exponential decay. However we also made the

assumption that the dot would have very strong Coloumb blockade, allowing only one electron in the dot. This assumption has not been met however, as we have more than one electron in the dot for all fields at lower entrance gates, and this persists until the said electron naturally decays out of the dot, figure 4.8.

This means the overall energy in the dot is completely different, and so the first-order equation will need a much bigger state space for the equation to become relevant, rather than the first order in the case of one electron. Looking at figure 4.11 it is clear that once the second and third electron have left the dot and there is only one electron to observe, the decay behaviour returns to being exponential. These behaviours can be in future by a willing theorist, part of the further work required to solidify the origin of this data behaviour.

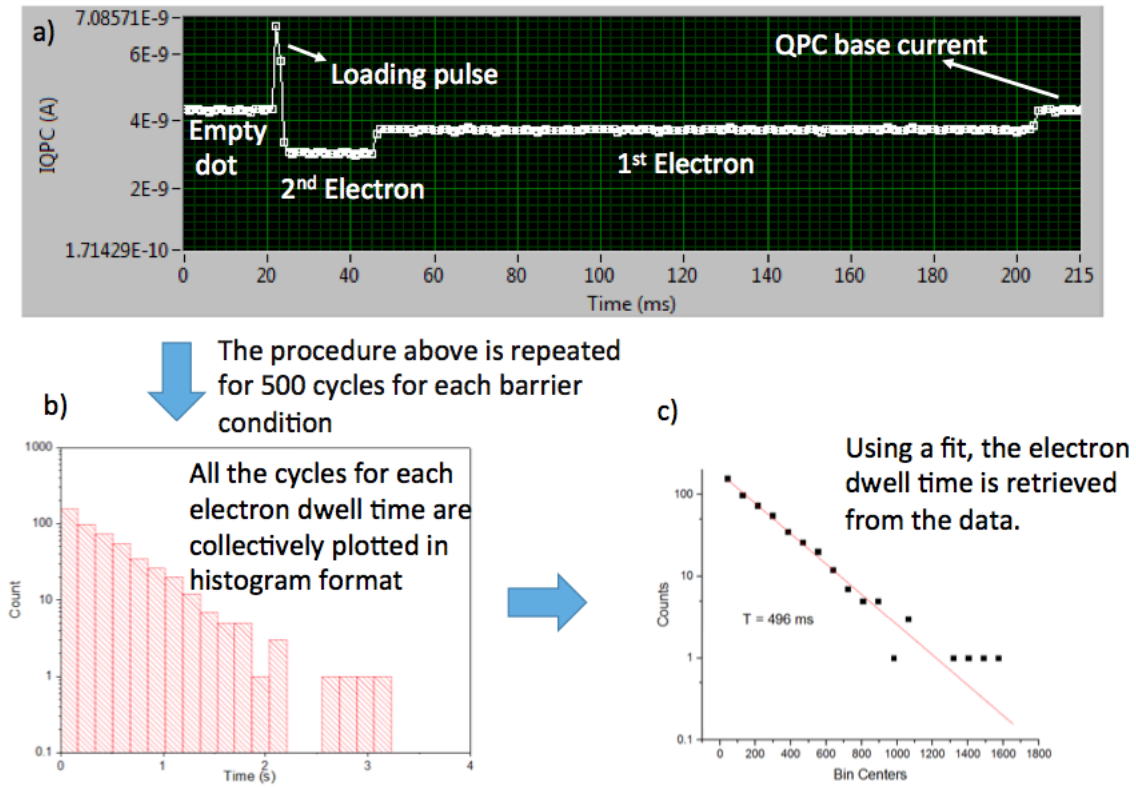

Figure 4.8: a)Readout from the Labview analysis program indicating the current through the QPC channel as the loading pulse loads two electrons into the dot, followed by the decay of the electrons out of the dot. b)Histogram produced using the readout time, taken for the first electron for all 500 cycles. c)Fit used to extract dwell time from the histogram data.

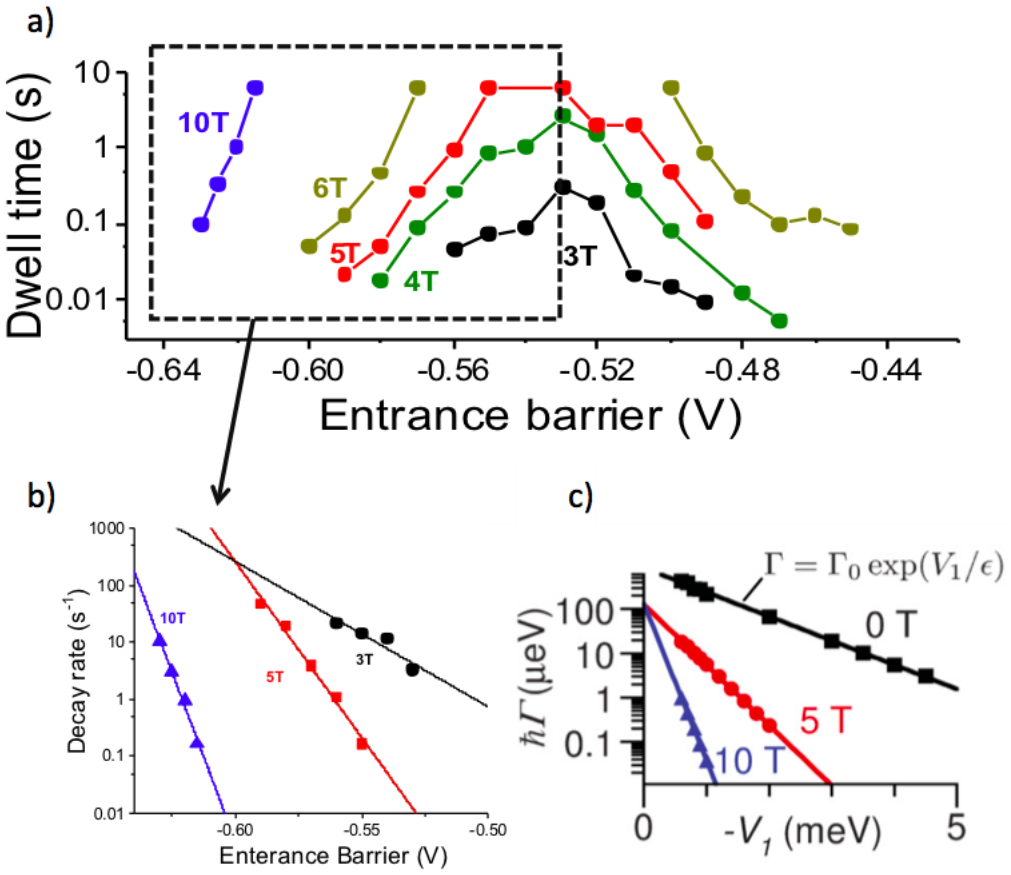

Figure 4.9: a)Electron dwell time in the dot at varying entrance gate voltages and magnetics fields. The exit barrier is set at constant voltage. b)Decay rate derived from the dwell time at 10T, 5T and 3T. c) Numerical data presented in the 2012 paper for comparison [110].

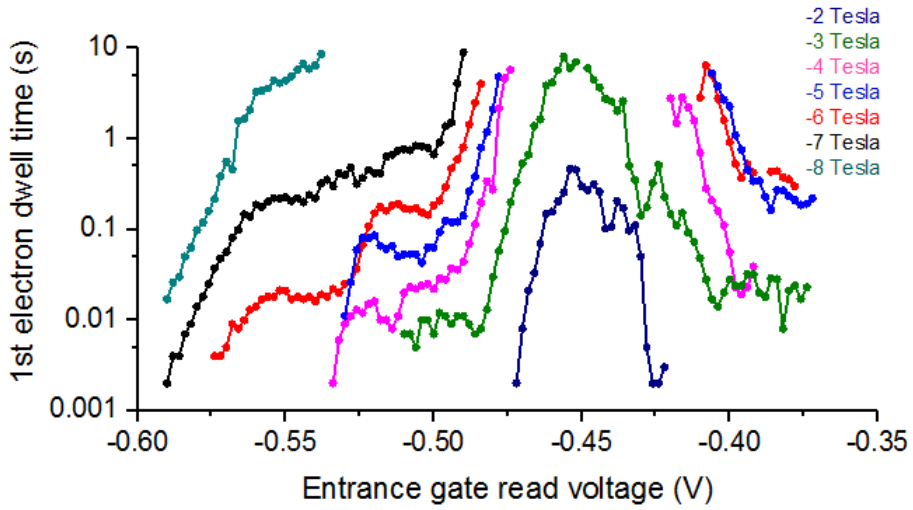

Figure 4.10: Dwell time measurement 8 months after the original experiment. Loading voltage for the entrance gate is set to -0.47V. Dwell times are shown for varying magnetic fields, with each point representing 500 cycles. The maximum experiment time was 10 seconds, after which each cycle would be terminated.

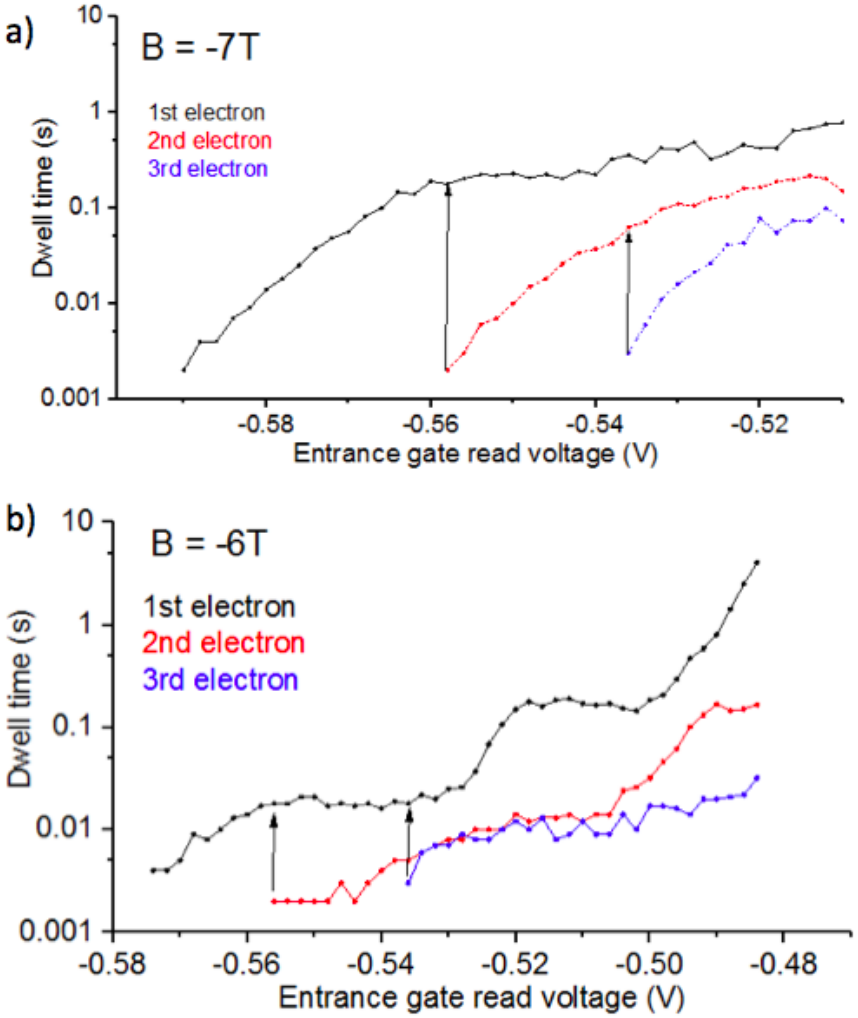

Figure 4.11: a)Dwell times for the first, second and third electrons leaving the dot at -7T. The arrows indicate points at which one of the three electrons has finally left the dot. b)Dwell times for three electrons at -6T.

4.4 Summary

This chapter discusses the operation of an electron pump - QPC device. The QPC gate is located outside the exit barrier between two ohmic contacts, creating a current channel capacitively coupled to the electron pump quantum dot. When current through this channel is sufficiently constricted, it is possible to probe the exact number of the electrons occupying the dot, and deriving a average time for the electrons remaining in the dot at various barrier heights. This is referred to as the dwell time, and it is investigated at varying magnetic field and barrier heights. We find that the number of electron present in the dot appear to effect the electron dwell times. Higher magnetic fields also increases the electrons dwell time within the dot, as well as the electrons occupancy becoming increasing more sensitive to changes made to the barrier heights.

Chapter 5

Electron pump single THz photon emission

One of the possible applications envisioned for the electron pump was its ability to act as a teraherts emitter. It was coupled with a QD device, meant to act as a detector. Ultimately this experiment was not performed due to lack of time. However the ground work is set for future endeavours into this investigation.

5.1 Fabrication of the QD detector

The quantum dot detector was also primarily fabricated at Chalmer's MC2 labs. The fabrication method used for this device is not dissimilar to the PC-QD device covered in chapter 6.

The major difference is introduced during the final EBL stage, when the finer gate patterns are exposed onto the device. Instead of the hook gate pattern created for the PC-QD device, see figure 6.2c, we expose the pattern of four gates used to create the QD. After patterning, the gates are metallised with layers of Cr and Au. This is followed by the final stage process discussed previously, and the finer mesa channel is exposed.

Figure 5.1 is an SEM image of the completed device, and its topological image obtained with an AFM.

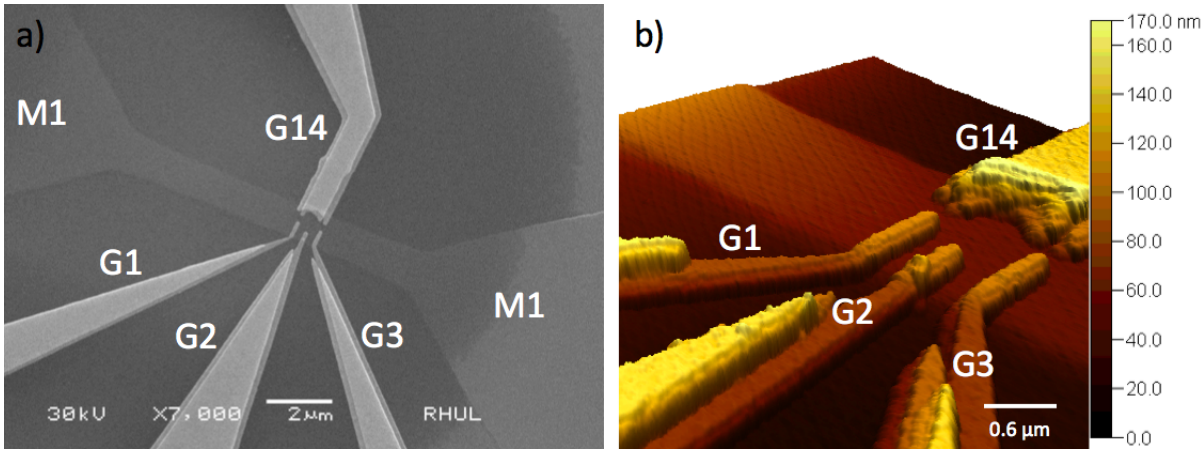

Figure 5.1: a)SEM of the quantum dot detector, where M1 refers to the mesa channel and G1, G2, G3 and G14 are the gates. b) AFM image of the device.

5.2 QD detector operation

The quantum dot (QD) detector, originally designed by Astafiev and Antonov [115], was utilised in detecting far-infrared (FIR) radiation. The QD is formed by negative bias applied to four gates over the 2DEG, figure 5.2.

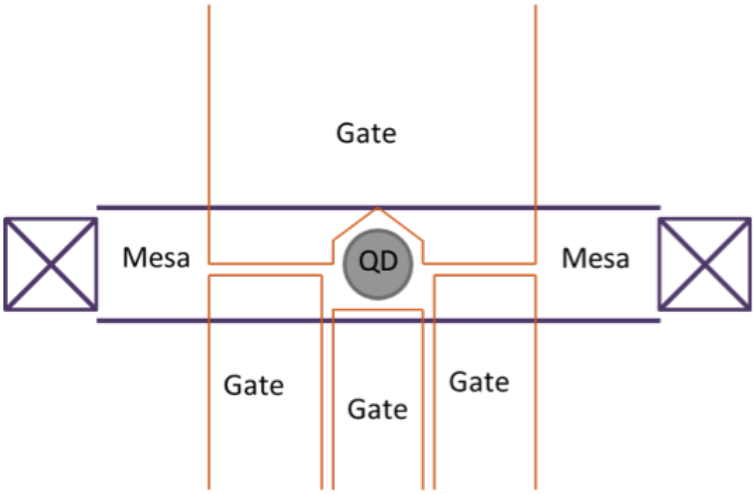

Figure 5.2: A simple sketch of the QD detector device, consisting of four gates and ohmic contacts. [115].

Applying magnetic (B) field, landua levels within the QD are observed, with the lowest orbital Landau level (LL0) and the first excited landau level (LL1) being our main points of interest. In figure 5.3, the outer ring and inner core form two separate compressible regions. Current through the QD displays Coulomb blockade oscillations.

LL0 is actively involved in the current transport and LL1 is only involved as far

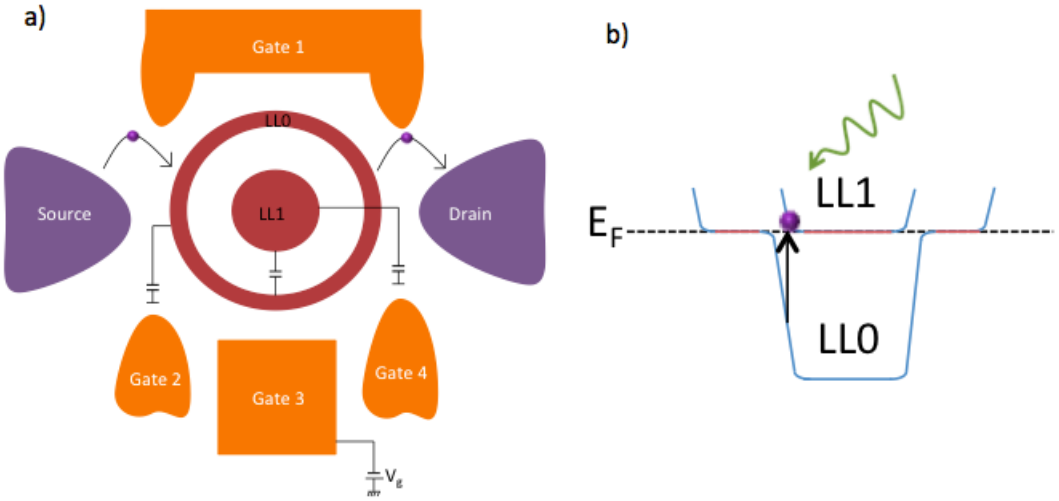

Figure 5.3: a) Formation of the lower Landau level (outer ring LL0) and higher excitation Landau level (inner core LL1). b) Electron jumping from LL0 to LL1, through photon absorption [115].

as it is capacitively coupled to LL0. LL0, is filled with two opposite spin polarities, and LL1 is partially occupied. At the Fermi level LL0 and LL1 form two compressed metallic regions. Tunnelling probability between the regions is suppressed by an insulating strip which is incompressible.

When the electrochemical potential of LL0, μ, lines up with the reservoirs we get conductance resonance since electrons are able to tunnel between the LL0 ring and electron reservoirs. The inner ring, LL1, contributes to this through its electrostatic coupling to LL0. The terahertz photon is absorbed by the QD, an electron is created in LL1 and a hole in LL0, figure 5.3. Eventually the electron would release its excess energy and drop back down to LL0. The extra electron leads the LL1 inner core to be negatively charged, affecting the outer LL0 level, as $-\Delta\mu_1 = \frac{eC_2}{C_2C_1+C_{12}C_1+C_2C_{12}}$. C_i and C_{ij}, where C_i and C_{ij} refer to capacitance between the two regions.

In this way LL1 has its over all charge polarity changed. This in turn can effect the current passing through LL0, by switching the current conductance either on or off. This polarisation causes a shift in the conductance resonance peaks, $-\Delta V_g\alpha - \Delta\mu_1$, figure 5.4. Alongside this, the electron in LL1 has a long life time due to the suppression of tunnelling out of this region. This makes the device ideal for terahertz detection [115].

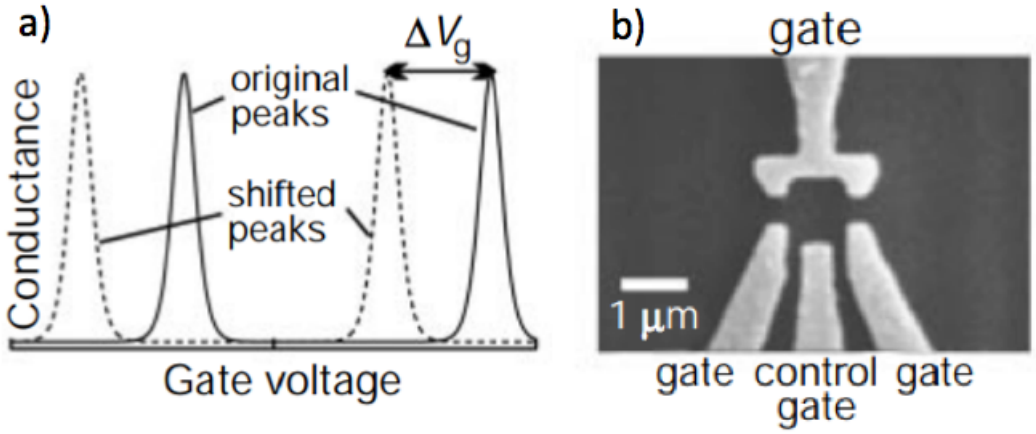

Figure 5.4: a) Coulomb conductance peaks as a function of gate voltage, V_g. The excitation of the electron from LL0 to LL1 leads to a shift in the conductance peaks. b) SEM of QD device, with four gates forming the QD in the 2DEG [115].

5.3 Emitter and detector combined set-up

Initially the Vericold system in the prior section was used, however, however due to a lack of magnetic field the experiment was moved to the Triton 200 dry dilution refrigerator. The set-up for the Vericold system is shown in figure 5.5, where the e-pump and QD detector were each encased in separate metallic containers, connected together via a circular wave-guide. The Triton 200 can be seen in figure 5.6.

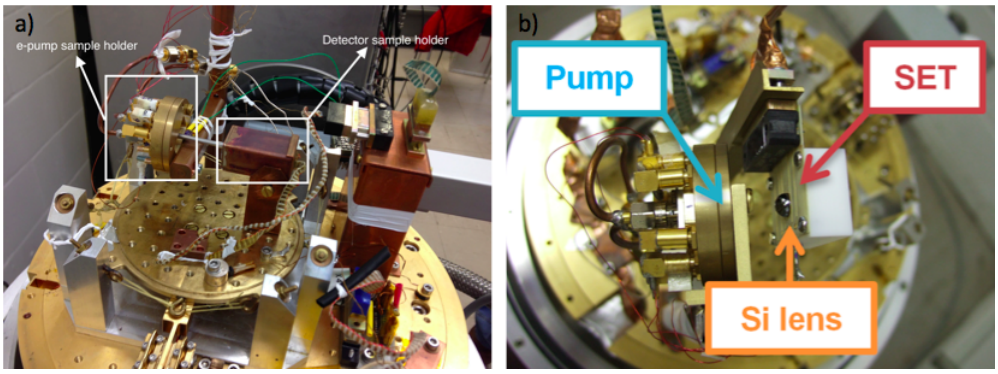

Figure 5.5: Two of the experimental set-ups: a)The electron pump and the detector are each enclosed in individual metallic sample holders, connected using a circular wave guide. b) The electron pump is enclosed in a circular metallic sample holder with a hole cut out in the centre facing the detector, which is encased in a white plastic container. It also has a hole cut out facing the pump, covered by a silicon lens.

The two metallic containers could not feasibly fit inside the sample puck of Triton

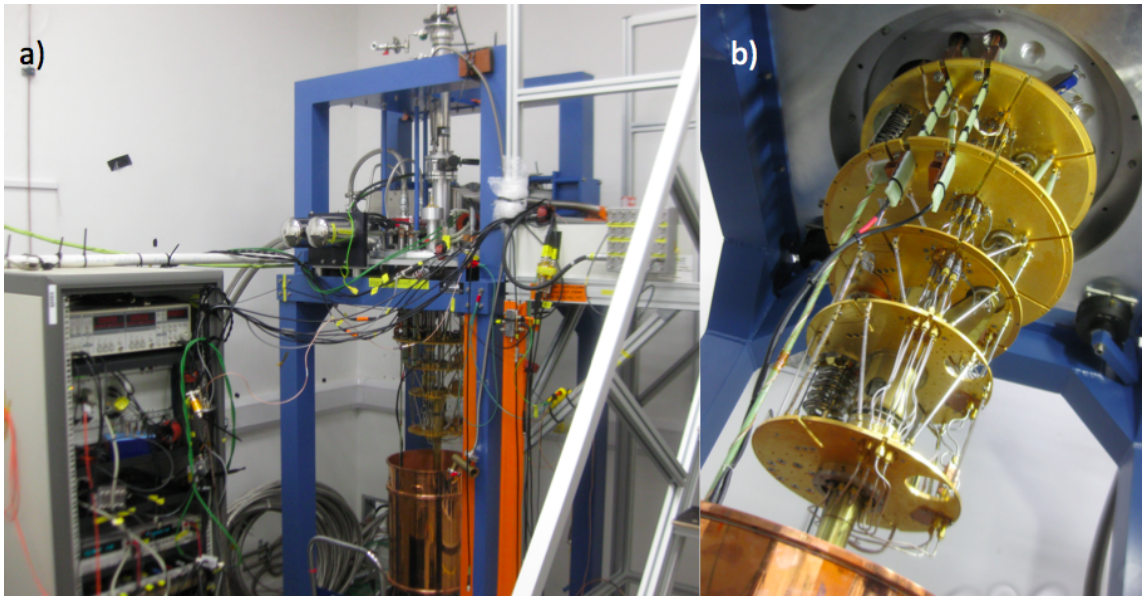

Figure 5.6: a) The Triton 200 prior to assembly before cool down b) a close up of the cooling stages.

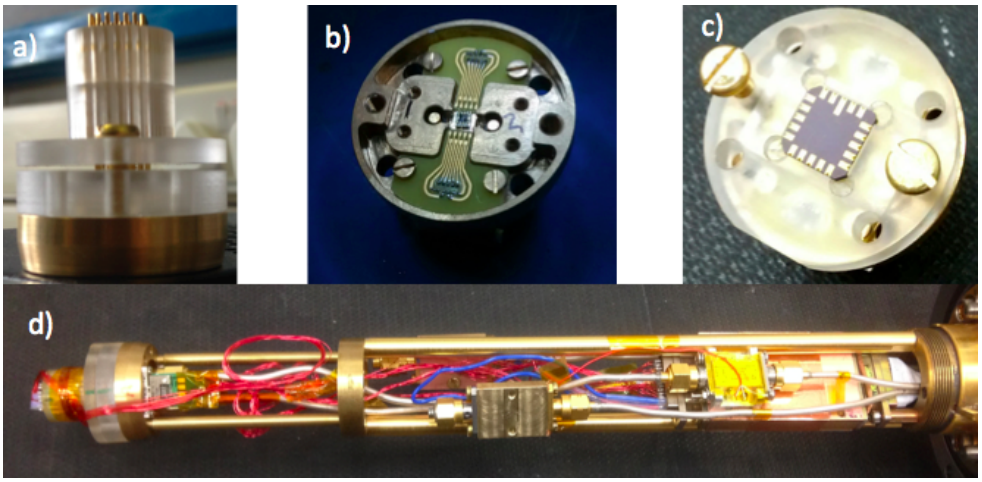

Figure 5.7: a) Newly designed dual sample holder fully assembled with b) the e-pump sample holder and c) the LCC sample holder to which QD detector is bonded. d) The sample holder assembled and connected to Triton 200 puck, ready to be loaded into the fridge.

200. This led to the design of a two sided sample holder that would meet our requirements for both the e-pump and the QD detector. The new sample holder, both in parts and fully assembled on the puck, can be seen in figure 5.7.

Taking a step back from the compact system, it's worth looking at the devices that would be fitted to either side of the new sample holder. Figure 5.8 shows the EBL (Electron Beam Lithography) design blue print for the electron pump device. It consists

of two electron pumps, connected through a central ohmic contact. Each has its own entrance (VG_1 and VG_3) and exit (VG_2 and VG_4) gates. In order to get reliable data, it is important for both e-pumps to be functioning well, as the shared ohmic contact can introduce the imperfections of one failed device to the other. During the experiment the most reliable electron pump is used while the other is blocked off using applied DC bias to pinch-off the channel.

The second device is shown in figure 6.5. This is a SEM pictures of the first detector (SET/QD), with the device bonded to a LCC package using aluminium bond wires. As it can be seen, each SET device is surrounded by a hook gate, in order to create a QD below each SET. The space between the two hook gates can also be used as a PC coupled to the QD. However this was not a viable alternative method of detection in our experiments, as we expect a single photon emission from the electron pump.

During the first measurements it became clear that the Coulomb blockade segment of the SET is heavily reduced when a magnetic field is applied, limiting the effectiveness of terahertz photon detection. An alternative device is used as a detector. Figure 5.9 shows the EBL blue print of this device, as well as an optical photo of the substrate, holding three devices.

5.4 Summary

The set-up for measuring possible terahertz emissions from the electron pump has been made by creating a two sided sample holder. One side fits the electron pump whilst the other has the QD detector facing the electron pump through a silicon filter in order to absorb any other undesirable radiation frequencies. But prior to using the QD in this experiment an SET-QD device was used. It was found that this device did not fit our measurement set-up as the SET did not function well under magnet field (a requirement for our pump measurements) due the a significant reduction in the coulomb blockade region. This meant that we switched over to using the QD detector device for this work. However due to lack of time this measurement will have to be carried out by another researcher.

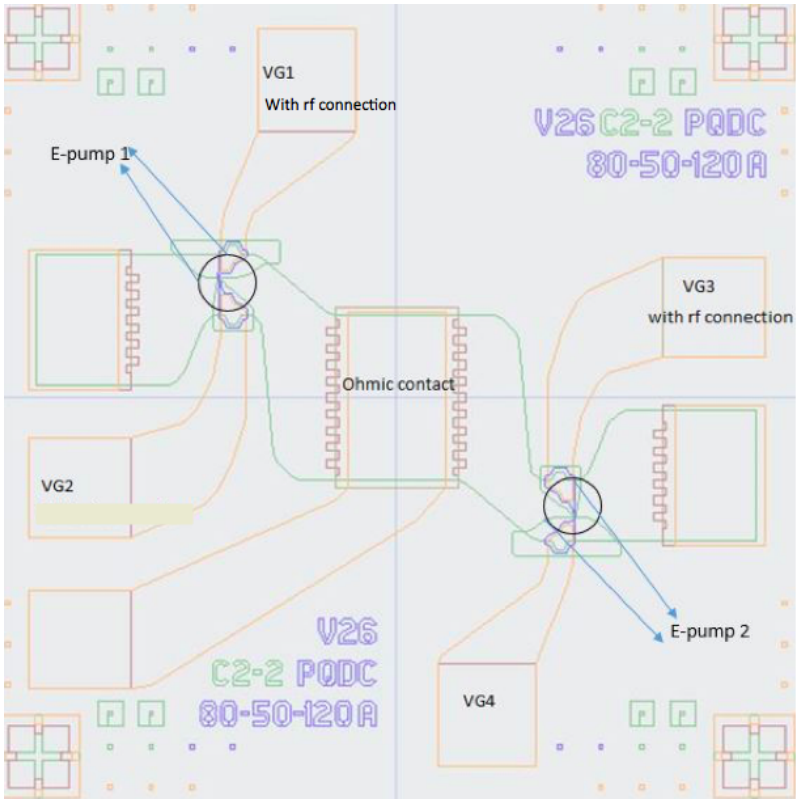

Figure 5.8: E-beam design for the electron pump substrate. Each substrate consists of two electron pumps which share an ohmic connection in the centre. For a stable experiment one must ensure that both electron pumps produce reproducible pump maps [107].

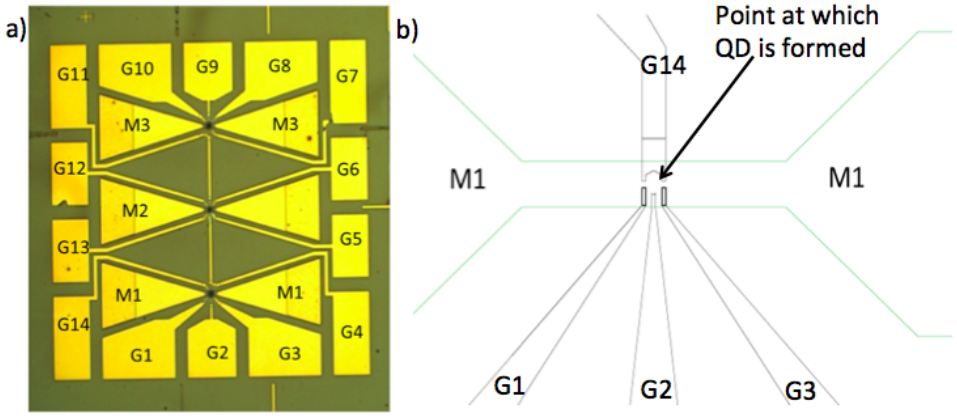

Figure 5.9: a) Optical image of the substrate with the new QD detectors. The mesa is labelled as M and gates are denoted as G. b) AutoCAD design close-up of one of the QDs devices, including the associated gates and mesa, with the QD formation point shown [116].

Chapter 6

THz imaging using PC-QD

6.1 PC-QD detector fabrication

Similar to the electron pump substrates, the PC-QD wafers are also grown using MBE. They were produced by XPERT semiconductors, based in Taiwan. Figure 6.1 shows the substrate structure, an AlGaAs/GaAs heterostructure with the 2DEG buried 90nm below the surface.

Once again a mesa channel is etched 100nm deep, using UVL to create the desired pattern. The wafer is wet etched. A second UVL is carrier out in order to create patterns for ohmic contacts. Before metal deposition, the exposed substrate surface is etched in a solution of HCl acid. The ohmic contacts themselves are made with a combination of E-gun evaporation of an adhesive Ni layer (15nm) and thermal evaporation of AuGe (150nm).

After deposition and lift-off of the Ni/AuGe contacts the wafers were annealed at 450°C for 40 seconds in Ar.

To further constrict the mesa channel, we use PMMA and EBL to expose the pattern. After development the wafer is selectively wet etched with a solution of $H_3PO_4 : H_2O_2 : H_2O$, with ratios of $4 : 2 : 94$.

The substrate is covered in Spin On Glass (SOG), T-12B. Using the EBL and developed in the MF319 solution once again the sample is patterned. The SOG layer serves as an insulator, preventing any current leakage from the metallic gates into the 2DEG.

Finally we move onto gate deposition. The sample is covered with double layer resist, 10% Copolymer and ZEP520. The sample is patterned by utilising the EBL, after which the wafer is developed in a solution of O-xylene followed by $IPA : H_2O$, $93 : 7$.

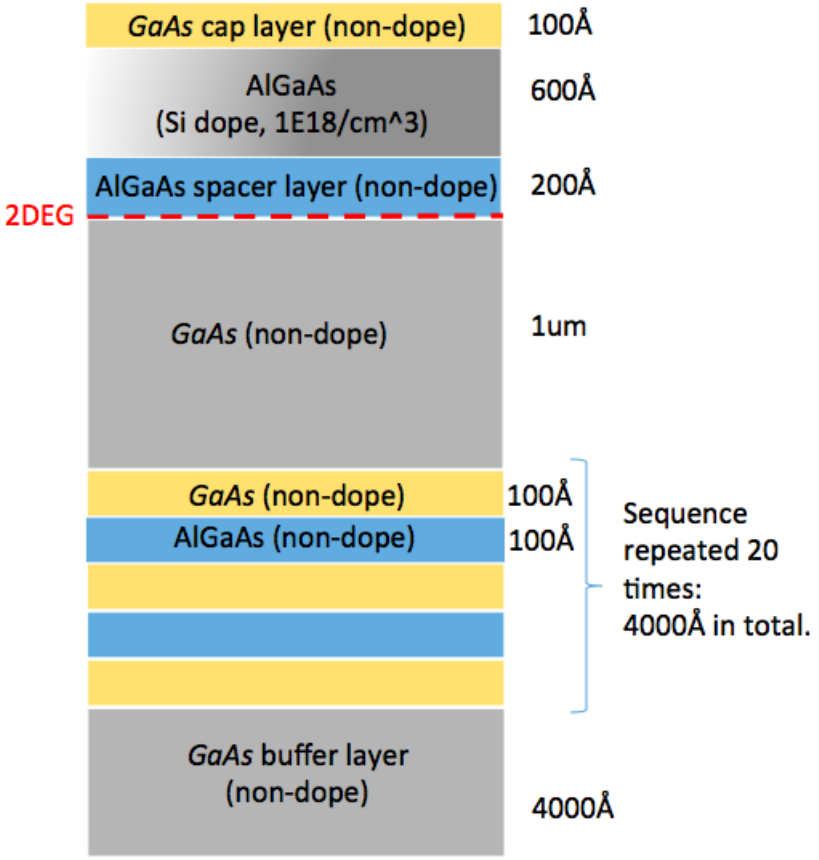

Figure 6.1: Cross sectional schematic of the PC-QD base substrate.

10nm of Cr is deposited followed by 100nm's of Au using a thermal evaporator. Finally acetone is used for the standard lift-off process. The finished device can be seen in figure 6.2 [117].

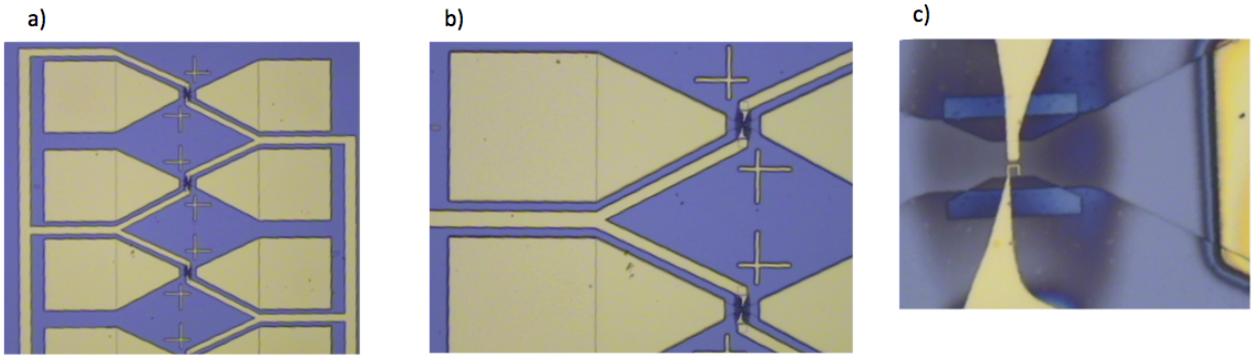

Figure 6.2: a) PC-QD device (b) and (c) zooming in. c) the hook gate is used to create the QD, and with the other gate can create ther point contacts constricted channel [117].

6.2 Fundamentals of PC-QD detectors

This detector consists of a narrow conductive channel formed in the 2DEG by negatively biased Au/Ti gates. The substrate is a GaAs/AlGaAs heterostructure with the 2DEG formed 90 nm below the surface with a carrier concentration of 1.45x10^{11} cm^{-2} and mobility of 1.2x10^5 cm^2/Vs at T=4.2 K. The focal point is a wide-band (0.2-2 THz) log-periodic metallic antenna, with a 1mm span. The gates, figure 6.3, also define two adjacent quantum dots which are made for the purpose of resonant excitation of plasma when a THz photon is absorbed [118]. Absorption of terahertz radiation leads to the resonant excitation of the plasma [119], which is then rectified further at the non-uniform potential profiles around the gates, leading to the offset *dc* voltage to appear across the conductive channel. Close to the pinch-off gate voltage, were the transconductance $\frac{dI_{bias}}{dV_{gate}}$ is large, this additional offset voltage gives rise to photocurrent [120].

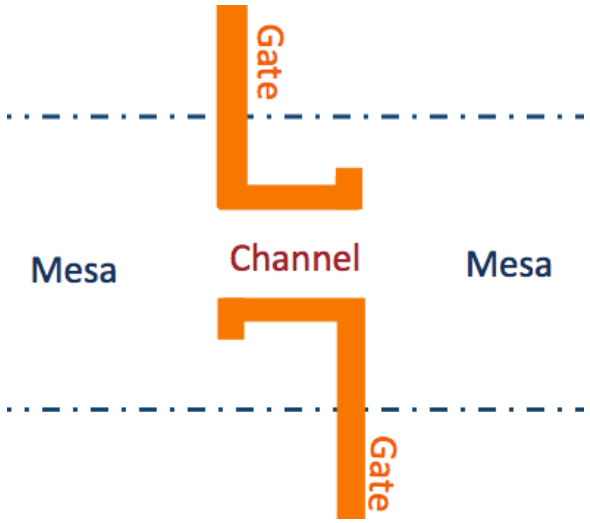

Figure 6.3: Basic PC-QD device. The THz sensor with two negatively biased metal gates, defining the conductive channel in the 2DEG of the GaAs/AlGaAs heterostructure mesa stripe.

This detector can be used for terahetz imaging, both transmitted and reflected. It should be noted in many applications, such as medicine or security, reflective imaging is of far more use rather than transmission imaging.

6.3 Experimental set-up

The point contact quantum system is utilised for terahertz imaging. An adiabatic demagnetisation refrigerator (ADR) is used for the study. The fridges optical window and filters

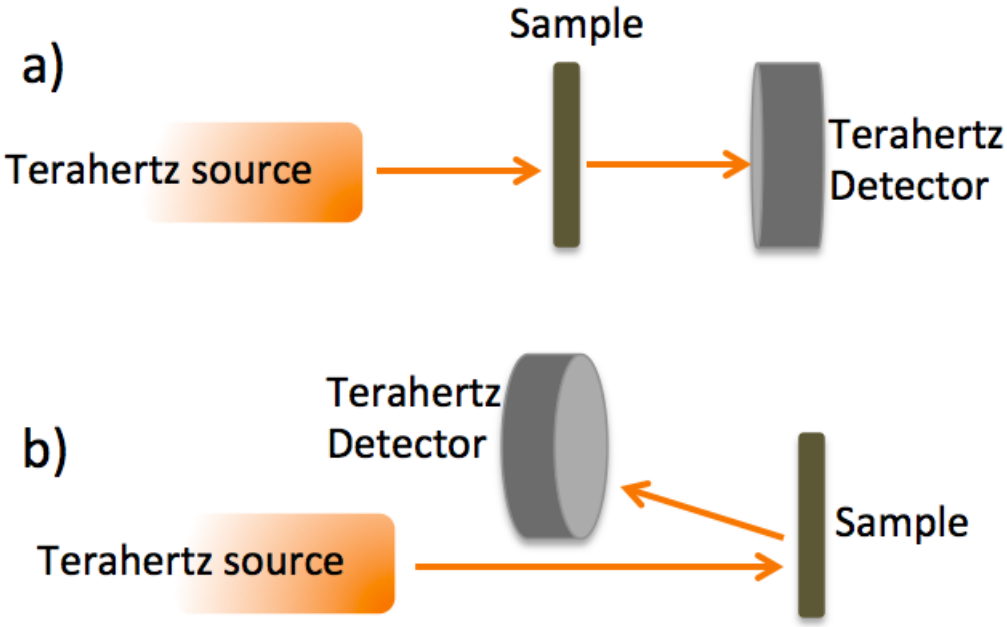

Figure 6.4: a) Transmission imaging, where the detector absorbs radiation that has successfully passed through the sample e.g. [121]. b) Reflection imaging, where the detector absorbs radiation that has been reflected from the sample e.g. [122].

are used to protect the low temperature stage from radiation. The terahertz source is placed outside the fridge during the experiment.

The Vericold system is a pulse tube refrigerator consisting of three stages. The temperatures achieved by the first and second stages are 70K and 4K respectively. The final stage with the detector reaches temperatures of approximately 300mK by utilising the demagnetisation properties of the stages.

Figure 6.5a shows an SEM image of the PC-QD device. The two hooked gates form a point contact (PC), whilst each hook individually forms a QD inside the 2DEG. The detector can be used for both transmitted and reflected imaging, with either a Gunn or resonant tunnelling diode as a terahertz source. Both methods are quite similar in experimental set-up as can be seen in figure 6.5b. It should be noted however, that in many applications of terahertz imaging, such as medicine or security, reflective imaging is of far more use than transmission imaging.

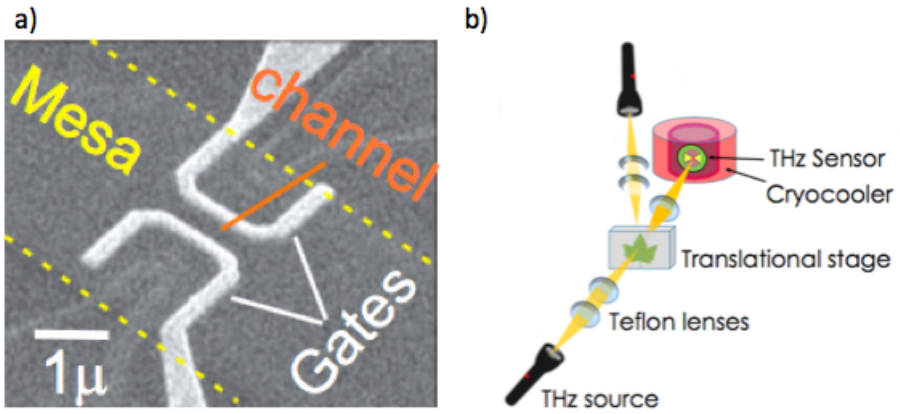

Figure 6.5: a) SEM image of THz sensor, the two negatively biased metal gates define the conductive channel in the 2DEG of the GaAs/AlGaAs heterostructure mesa stripe. b) Possible set-up for an imaging experiment using the PC-QD device as a detector. THz radiation is focused on the object on the translation stage, and is then transmitted/reflected towards the cryogenic sensor.

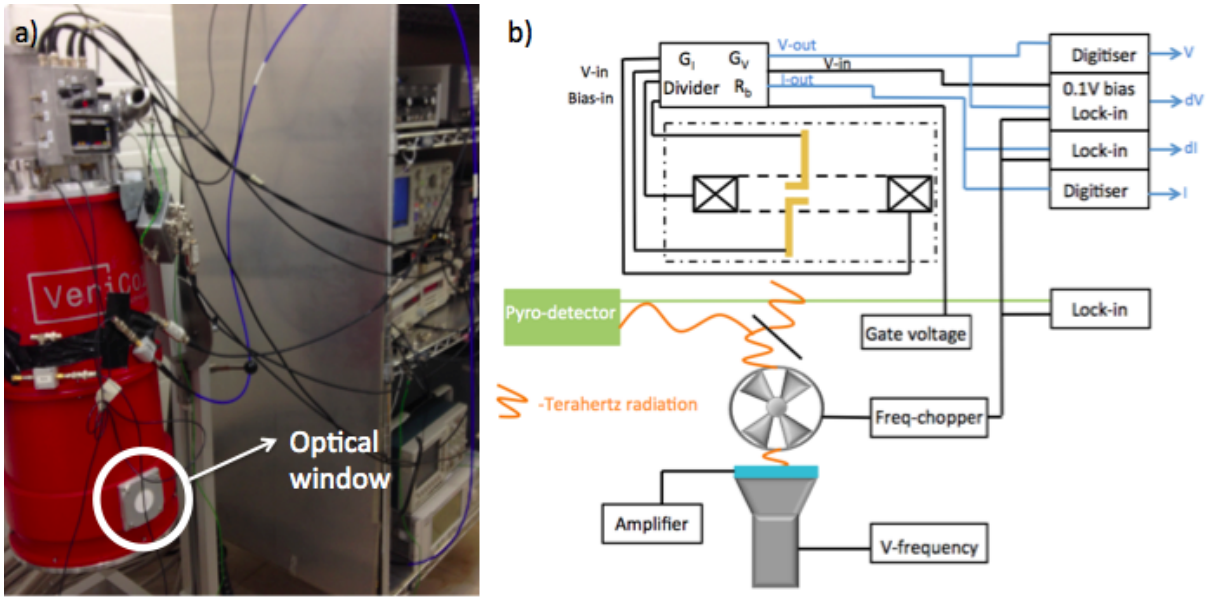

Figure 6.6: a)The Vericold, with markers labelling the position of the optical window, allowing the source to successfully expose the drain to an shower of terahertz radiation b) Schematic of set-up used for imaging.

6.4 THz imaging

In this work we report operation of the PC-QD device for imaging of room temperature objects. We take images of an ivy leaf in transmission and reflection modes by using spectral sources, the Gunn diode and the resonance tunnelling diode. The reflection image is of particular importance as it indicates feasibility of an active remote imaging

system with a spectral source and detector. In order to ease the need for bulky cryogenic equipment for the imager, we study operation of the detector up to temperatures where the compact cryocoolers are readily available now, >50K. The detector itself is a narrow conductive channel formed in the two dimensional electron gas (2DEG). It has responsivity of 10mA/W at 0.5K, with a steady decrease to 0.1mA/W at 50K. It is scaleable, spectrally selective and robust in operation. With an optimal choice of material we envisage operation of the detector for imaging purposes at temperatures above 77K.

The experimental setup is shown in figure 6.5b. We use two spectral sources for illumination, a frequency doubler for the Gunn diode with 2mW at 177GHz, or the resonance tunnelling diodes (RTDs) at 536GHz and 556GHz with the nominal power of 5μW and 10μW respectively. The optical system collimates radiation on the leaf fixed at the X-Y translation stage, and then focuses the transmitted/reflected beam to the detector in the cryocooler. There are a set of four filters in the cryocooler between room temperature and the cold stage with a steep attenuation of radiation of wavelength shorter than 30μm. The attenuation for the radiation of interest, λ ~200μm, is 35dB. The detector is a narrow conductive channel formed in 2DEG by negatively biased metal gates at the top of the GaAs/AlGaAs heterostructure, see figure 6.5a. The pattern is in a focal point of wide-band, 0.2-2THz, log-periodic metallic antenna of mm span. The plasma waves are resonantly excited in the 2DEG by absorption of terahertz radiation [119]. The plasma waves are further rectified at the non-uniform potential profile around the gates so that the offset dc voltage appears across the conductive channel. Close to the pinch-off of the channel this additional offset voltage gives rise to a photocurrent. A typical pinch-off curve of the channel current, I_{bias}, and the photocurrent, I_{ph}, are shown in figure 6.7. A bias voltage of V_{bias}=15 μV is applied across the channel. Close to the pinch off there are almost periodic oscillations of the I_{bias} and I_{ph} shifted by π with each other. They originate from the Coulomb blockade of the current due to an accidental quantum dot formed in the long conductive channel [120].

The transmission image of a leaf, I_{ph}(x,y), is shown in figure 6.8. The leaf is fixed at the translation stage, placed 50cm from the sensor at room temperature. The RTD at 556GHz of a nominal output power of 10μW is used as the source of terahertz radiation. The amplitude of variation of the photocurrent in the image is 25pA.

RDTs are possible sources in terahertz remote spectral imaging systems as they are compact, robust and reliable. The output power has been raised substantially during

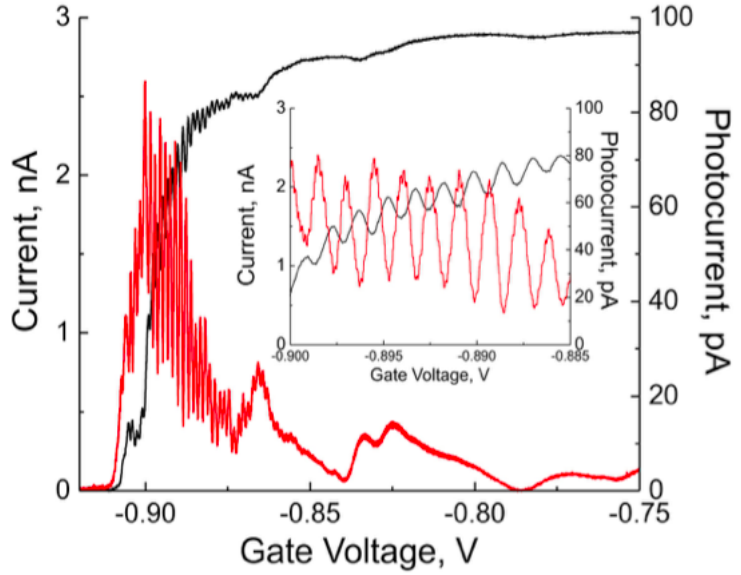

Figure 6.7: a)Bias current and the photo-current of the conductive channel. The photo-current appears under terahertz radiation of a Gunn source of 0.75mW output power. It has a maximum close to the pinch-off of the channel. Insert: the blow up of curves close to the pinch-off reveals the periodic oscillations of the bias current and the photo-current, which are shifted by π with respect to each other. The data was taken at 0.7K.

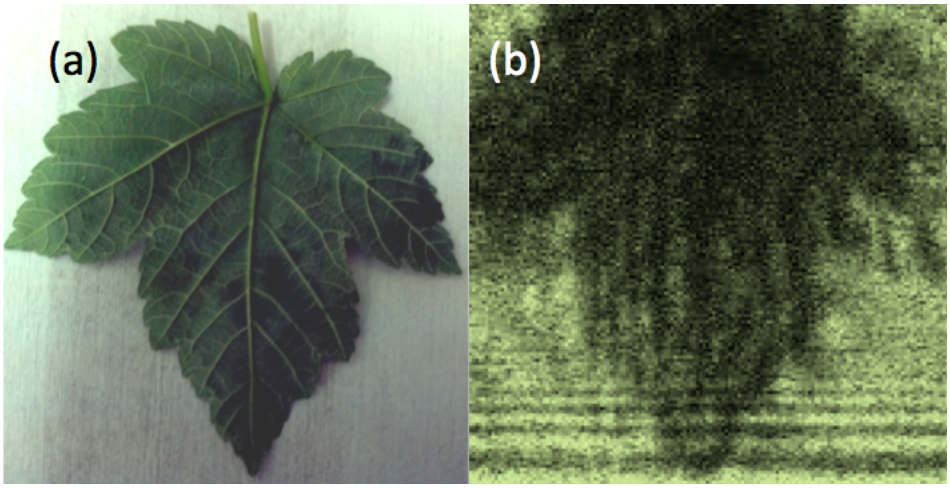

Figure 6.8: Optical and terahertz transmission image of the maple leaf taken by using the RTD of 556GHz with a nominal power 10μW as a source. The maximum amplitude of I_{phmax} is 35pA, the contrast $(I_{phmax} - I_{phmin})/I_{phmax} = 0.75$. The sensor is kept at T=0.7K

last few years, particularly at low frequencies. Thus devices operating at 305GHz with the output power up to 3.5mW have been reported [123]. However the power is still low at higher frequencies, typically below 50μW above 500GHz. Recently there was a

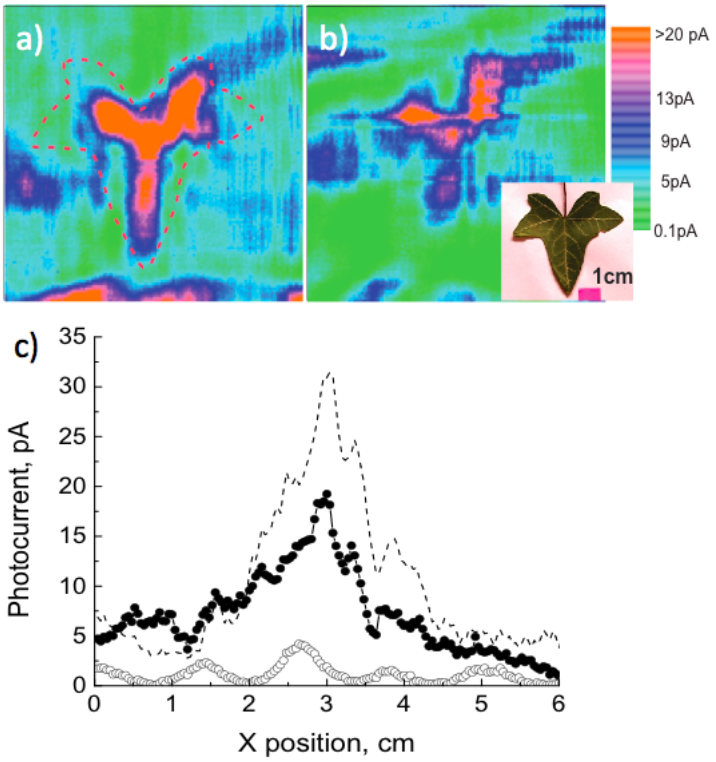

Figure 6.9: a) Reflective THz image of an ivy leaf, left, b) reflective image of the leaf hidden in a paper envelope. The detector is at 0.7K for both cases. c) individual traces of the left image (dashed), right image (filled circles), and the trace taken when detector is at 6K (empty circles).

breakthrough in development of terahertz generators using stacked Josephson Junctions in $B_2Sr_2CaCu_2O_8$ high temperature superconductors. These can deliver up to 1mW [124]. The factors affecting application of these sources are the need for cryogenic temperatures, $T < 70K$, and limited frequency tunability. The latter is because the operation frequency is determined by the geometrical sizes of the resonator, which is cut out of the $B_2Sr_2CaCu_2O_8$ material. The Josephson Junction generators made of $YBa_2Cu_3O_7$ superconductors allow for frequency tuning, however the output power of these sources is smaller than $1\mu W$ [125].

In most of prospective commercial uses, such as medicine or security, one needs a reflective, rather than transmission, spectral image. We have carried out experiments with the reflective images. The set-up is similar to the transmission measurement shown in figure 6.5b. We use 177GHz Gunn diode source at maximum power of 2mW. Reflective terahertz images of an ivy leaf, and the reflective image of the same leaf hidden in a paper envelope are shown in figure 6.9a. When the paper sheet covers the leaf the signal drops by 40%. The image also depends on the flatness of the object: the signal is weaker at the

edges where the leaf is corrugated. Individual scans across the x-axis are shown in figure 6.5c. The amplitude of the signal is relatively high, up to 30pA. It drops by a factor of 6 when the temperature of the detector increases from 0.7K to 6K. A further increase of the detector temperature has a weaker effect on I_{ph}, which is discussed later.

In these experiments we kept the detector at the lowest temperatures, T<1K, in order to have high levels of detected photocurrent. However for the wider applications one needs a detector operating at much higher temperatures, T>50K, where compact cryocoolers are readily available. In this section, we are concerned about the feasibility of high temperature operation of plasmon detectors based on 2DEG heterostructures. The gated two-dimensional electron gas has been the subject of a number of works related to terahertz technologies. The rectification of plasma waves and direct bolometric effects were observed with the point contact detectors operating below 4K at 1.5THz at Buffalo University [126, 127]. At high power, above 20mW, a continuous source of terahertz radiation was used in the experiments. The photosensitive spectral operation of gated 2DEGs in a wide temperature range, from 4K to 180K, was reported by another group [128]. Their study focused on the lower end of terahertz spectrum, around 100GHz. We positioned our detector in between the frequency range of 0.1THz and 1.5THz, where potential applications for the spectral terhertz imager are envisaged. The detector is made of a GaAs/AlGaAs heterostructure with the 2DEG formed 90nm below the surface, and carrier concentration of 1.45x10^{11} cm^{-2} with mobility of 1.2x10^5 cm^2/Vs at T=4.2K.

Two negatively biased metal gates over the heterostructure define a narrow conductive channel between them, as well as two adjacent quantum dots, see figure 6.5a. They are made for the purpose of resonant excitation of plasma waves in the QDs when a THz photon is absorbed. The rectification of these plasma waves can be detected by the narrow conductive channel [120]. The photoresponse is largest at low temperatures, see figure 6.10a, falling by almost three orders of magnitude when the detector temperature increases from 0.7K to 50K. The photocurrent has the steepest gradient in the range of 0.5K to 2K, where the suppression is slowed down.

Overall the photo-response curve follows the transcurrent gradient $\partial I_{bias}/\partial V_g$ of the narrow conductive channel. This is largest at the maxima of $\partial I_{bias}/\partial V_g$. However, this is violated by periodic oscillations, figure 6.7: oscillations of I_{ph} are shifted by by $\pi/2$ with respect to $\partial I_{bias}/\partial V_g$. Another property of I_{ph} is a weak sensitivity to V_{sd}. This observation is in contrast to the experiments of Song et al. [127], where the photo-response

current had a strong dependence on V_{sd}. The latter may be attributed to the bolometric effect.

The photosensitive operation of the device can be modlled by a phenomenological model. The photocurrent arises due to an additional potential in the conductance channel close to the PC, ∂V_{sd} and at the gate, ∂V_g, due to rectification of the terahertz radiation absorbed [126]:

$$I_{ph} = \alpha(\partial^2 I_{bias}/\partial V_g \partial V_{sd}) + \beta(\partial^2 I_{bias}/\partial {V_g}^2) \tag{6.1}$$

where $\alpha = \langle \delta V_g \delta V_{sd} \rangle$ and $\beta = 1/2\langle \delta {V_g}^2 \rangle$. α and β can be used as fitting parameters. We approximated the photo-response at different temperatures. $\langle \delta V_{sd} \rangle$ was found to be 1 - 30μV with minor contributions from $\langle \delta V_g \rangle$, see figure 6.10b. δV_{sd} has a steep drop from 0.5K to 2K, then it decreases with a lower gradient.

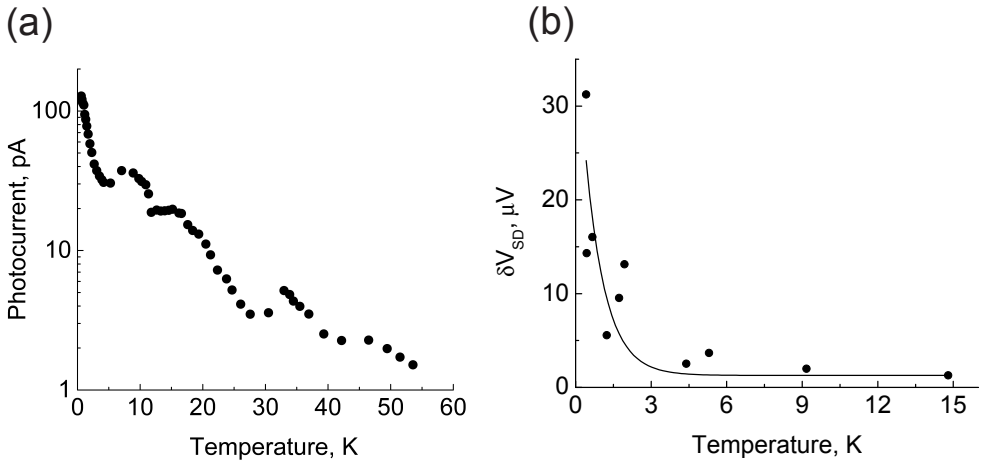

Figure 6.10: (a) Maximum photocurrent at different temperatures. The amplitude is suppressed by two orders of magnitude at higher temperatures. (b) Temperature dependance of the photo-induced δV_{sd}. It has a sharp drop between 0.5 K and 4 K. Then the decrease of δV_{sd} is flattened out. The solid line is an approximation using the exponential decay function.

There are two mechanisms suggested in order to explain the induced $\langle \delta V_{sd} \rangle$ and $\langle \delta V_g \rangle$. One refers to the rectification of the plasma wave induced in the 2DEG [128, 129], while an alternative explanation concerns the bolometric response of the PC [127]. If we assume that the photo response has an origin in excitation of plasma waves, then we should expect that the amplitude of plasma waves, and correspondingly δV_{sd}, would be suppressed by the exponential factor $\exp(-\omega\tau(T))$, where $\tau(T)$ is the temperature dependent scattering time of the electrons, and ω is the plasma wave frequency. $\tau(T)$ decreases

at higher temperatures, and correspondingly the photo-response should be suppressed. From the fitting of $\delta V_{sd}(T)$ in figure 6.16b with the exponential suppression factor, we find $\tau(0.5K)/\tau(45K)$ ≈3.5. However the same ratio calculated from the transport measurements is much smaller. We use the Drude formula and calculate the conductance and the electron's scattering time $G(0.5K)/G(45K)=\tau(0.5K)/\tau(45K)$ ≈1.35 assuming that the 2DEG carrier concentration is constant. The shape of $\tau(T)$ incurred from the photo-response is also different from that derived from the conductance: it drops faster at temperatures up to 2K, but it decays much slower at higher temperatures. Thus we observe photo-response up to 50K, where the excitation of coherent plasma waves should be more strongly suppressed, if we start with the amplitude of the effect at 2K. The plasmonic operation of GaAs/AlGaAs devices have also been seen at temperatures of 150K [130]. So far there is no clear explanation for these observations. The other road to increase the operation temperature of the terahertz detectors is in utilising materials with higher mobility and a carrier concentrations at high temperatures. Recently a graphene field-effect terahertz detector operating at room temperature has been reported [131].

6.5 Summary

We demonstrated the capability for performing transmission and reflection terahertz imaging using a detector with a narrow conductive channel in GaAs/AlGaAs. The detector has 0.01A/W responsiveness when cooled to 0.5K. The sensitivity decreases by two orders of magnitude, when the temperature increases to 50K. We modelled the photoresponse: there is a exponential drop in sensitivity when temperature is raised to 6K, however a further decrease of the photoresponse is slowed down. This may open the possibility for spectral remote imaging with a choice of the detector material and powerful enough emitters.

Chapter 7

Conclusion and further work

We present studies of electron behaviour in the dynamic quantum dot formed in the electron pump, and the possibilities present to utilise these behaviours as tools for terahertz detection and emission. The electron loading and pumping through the quantum dot, was investigated at field where the dot is clearly defined and isolated from the source and drain. Here it behaves as an artificial atom with distinct energy levels for the incoming electrons to occupy. Quantised currents with excited states were obtained at varying fields and the F-D spectrum was fitted, base on the prediction that the dot potential is circular and symmetric in nature. From this $\hbar\omega_o$ was found to be $\approx$ 5meV, translating to 1.21THz of frequency, well within the low energy terahertz range.

The pumps shows suitability as a possible emitter, as we see that at 4T and 500MHz of frequency applied to the dots entrance barrier, electrons are loaded into an excited level, and as a result tunnel through the exit barrier before the electrons in the ground state have been pumped through. We demonstrated that using an AWG this electron could be relaxed down to the ground state. We designed and built a double sided sample holder to hold both the electron pump and the QD detector that would be used to detect any emitted terahertz photon.

The electron pump was also fabricated with the addition of a quantum point contact gate that was placed outside the exit barrier. This gate can pinch off the current channel flowing outside the exit gate, which is capacitively coupled to the electron pump quantum dot. We created a low noise experiment system, allowing us to observe the number of electrons occupying the dot clearly and distinguish them with inconsequential error margins. We created software necessary to carry out studies on electron dwell times in the dot and

analyse the data to 2ms accuracies. This allowed us to mapped out the electron dwell times at varying fields, which can be compared to electron dwell times under terahertz radiation to study the electron pump as a detector. The cryostat probe was re-designed and re-assembled to include a wave-guide, directing terahertz radiation from it's room temperature source to the dynamic quantum dot at low temperatures, overcoming all technical difficulties introduced by this challenging assembly.

The dwell times in the electron pump followed theoretical predictions and decayed exponentially out of the dot, with the decay rate becoming more sensitivity to barrier height as the magnetic fields were increased. However this changed when a second more detailed study of the electron pump was carrier out, with flat plateaus appearing at various points of the decay. This is a result of more than one electron occupying the dot, changing the overall energy of the system and shape of the first electrons decay rate. The first electron starts to decay exponential once it is the last remaining electron in the dot. Future work on this device will have to focus on theoretical mapping of the supplied theory and introduction of the applied terahertz photons to the detection experiment. This would ideally lead to plotting of electron dwell time in the dot in the presence of radiation, and make a comparison to data taken in its absence. The two comparative experiments will be performed with the same electron number present in both cases (ideally 1 for simplicity). Further investigation will also have to be done to ensure any change in the dwell time in the presence of radiation is as a result of photo absorption rather than heating of the dot.

We also demonstrated the capability for performing transmission and reflection terahertz imaging using a detector with a narrow conductive channel in GaAs/AlGaAs (PC-QD detector). The detector has 0.01A/W responsiveness when cooled to 0.5K. The sensitivity decreases by two orders of magnitude, when the temperature increases to 50K. We model the photoresponse: there is a exponential drop of sensitivity when the temperature is raised to 6K, however a further decrease of the photoresponse is slow down. This may open a possibility of spectral remote imaging with a choice of the detector material and the powerful enough emitters.

Bibliography

[1] Collins English Dictionary. Definition of metrology.

[2] K. v. Klitzing, G. Dorda, and M. Pepper. New method for high-accuracy determination of the fine-structure constant based on quantized hall resistance. *Physical Review Letters*, 45:494, 1980.

[3] B.D. Josephson. Possible new effects in superconductive tunnelling. *Physics Letters*, 1:251–253, 1962.

[4] K. K. Likharev and A. B. Zorin. Theory of the bloch-wave oscillations in small josephson junctions. *Journal of Low Temperature Physics*, 59:347–382, 1985.

[5] F Piquemal and G Geneves. Argument for a direct realization of the quantum metrological triangle. *Metrologia*, 37, 2000.

[6] Neil M Zimmerman and Mark W Keller. Electrical metrology with single electrons. *Measurement Science and Technology*, 14, 2003.

[7] B N Taylor. Impact of quantized hall resistance on si electrical units and fundamental constants. *Metrologia*, 21, 1998.

[8] Mark David Blumenthal. *Gigahertz Quantised Charge Pumping*. PhD thesis, Wolfson College, University of Cambridge, 2007.

[9] K.K. Likharev. Single-electron devices and their applications. *Proceedings of the IEEE*, 87:606 – 632, 1999.

[10] S.P. Giblin, M. Kataoka, J.D. Fletcher, P. See, T.J.B.M. Janssen, J.P. Griffiths, G.A.C. Jones, I. Farrer, and D.A. Ritchie. Towards a quantum representation of the ampere using single electron pumps. *Nature Communications*, 3:930, 2012.

[11] M. D. Blumenthal, B. Kaestner, L. Li, S. Giblin, T. J. B. M. Janssen, M. Pepper, D. Anderson, G. Jones, and D. A. Ritchie. Gigahertz quantized charge pumping. *Nature Physics*, 3, 2007.

[12] Samuel James Wright. *Quantised charge pumping in a perpendicular magnetic field.* PhD thesis, Wolfson College, Cambridge, 2010.

[13] K. Ikushima and S. Komiyama. Imaging by terahertz photon counting comptage de photons pour l'imagerie térahertz. *Comptes Rendus Physique*, 11:444–456, 2010.

[14] M. Dell'Anna, V. Antonov, D. Bagliani, M. Biasotti, J.L. Coutaz, F. Gatti, M. Kiviranta, S. Kubatkin, E. Otto, M. Sypek, and S. Spasov. Thz spectroscopy using low temperature mesoscopic devices. *Journal of Low Temperature Physics*, 167:467–472, 2012.

[15] B. B. Hu and M. C. Nuss. Imaging with terahertz waves. *Optics Letters*, 20:1716–1718, 1995.

[16] T. Loffler, T. Bauer, K.J. Siebert, H.G. Roskos, A. Fitzgerald, and S. Czasch. Terahertz dark-field imaging of biomedical tissue. *Optics Express*, 9:616–621, 2001.

[17] Bradley Ferguson, Shaohong Wang, Doug Gray, Derek Abbott, and X-C Zhang. Towards functional 3d t-ray imaging. *Physics in Medicine and Biology*, 47:3735, 2002.

[18] Lu. Meihong, Shen. Jingling, Li. Ning, Zhang. Yan, Zhang. Cunlin, Liang. Laishun, and Xu. Xiaoyu. Detection and identification of illicit drugs using terahertz imaging. *Journal of Applied Physics*, 100, 2006.

[19] Y.C. Shen, T. Lo, P.F. Taday, B.E. Cole, W.R. Tribe, and M.C. Kemp. Detection and identification of explosives using terahertz pulsed spectroscopic imaging. *Applied Physics Letters*, 86, 2005.

[20] M. Inuzuka, Y. Kouzuma, N. Sugioka, K. Fukunaga, and T. Tateishi. Investigation of layer structure of the takamatsuzuka mural paintings by terahertz imaging technique. *Journal of Infrared, Millimeter, and Terahertz Waves*, 38:380–389, 2017.

[21] A. Doria, G. P. Gallerano, E. Giovenale, A. Casini, C. Cucci, M. Picollo, M. Poggesi, L. Stefani, K. Fukunaga, and M. Tamassia. Vis-nir hyperspectral and terahertz imaging investigations on a fresco painting on tavella by alessandro gherardini. *Journal of Infrared, Millimeter, and Terahertz Waves*, 38:390–402, 2017.

[22] Peter H. Siegel. Terahertz technology. *IEEE Transactions on Microwave Theory and Techniques*, 50, 2002.

[23] E. J. Nichols and J. D. Tear. Joining the infrared and electric wave spectra. *Astrophysics Journal*, 61:17–37, 1925.

[24] J. W. Fleming. High resolution submillimeter-wave fourier-transform spectrometry of gases. *IEEE Transactions on Microwave Theory and Techniques*, MTT-22:1023–1025, 1974.

[25] D. Leisawitz et al. Scientific motivation and technology requirements for the spirit and specs far-infrared/submillimeter space interferometers. *Proceedings of SPIE*, 4013:36–46, 2000.

[26] D. F. Santavicca, B. Reuletb, B. S. Karasikc, S. V. Pereverzevc, D. Olayad, M. E. Gershensond, L. Frunzioa, and D. E. Prober. Characterization of terahertz singlephotonsensitive bolometric detectors using a pulsed microwave technique. *AIP Conference Proceedings*, 1185, 2009.

[27] D. F. Santavicca, B. Reulet, B. S. Karasik, S. V. Pereverzev, D. Olaya, M. E. Gershenson, L. Frunzio, and D. E. Prober. Energy resolution of terahertz single-photon-sensitive bolometric detectors. *Applied Physics Letters*, 96, 2010.

[28] P. R. Lawson, A. Ahmed, R. O. Gappinger, A. Ksendzov, O. P. Lay, S. R. Martin, R. D. Peters, D. P. Scharf, J. K. Wallace, and B. Ware. Terrestrial planet finder interferometer technology status and plans. *Proceedings of SPIE*, 6268, 2006.

[29] S. S. Dhillon et al. The 2017 terahertz science and technology roadmap. *Journal of Physics D*, 50, 2017.

[30] W. Knap, Y. Deng, S. Rumyantsev, and M. S. Shur. Resonant detection of subterahertz and terahertz radiation by plasma waves in submicron field-effect transistors. *Applied Physics Letters*, 81, 2002.

[31] W. Knap, V. Kachorovskii, Y. Deng, S. Rumyantsev, J.-Q. Lü, R. Gaska, and M. S. Shur. Nonresonant detection of terahertz radiation in field effect transistors. *Journal of Applied Physics*, 91, 2002.

[32] W. Knap, Y. Deng, S. Rumyantsev, J.-Q. Lu, and M. S. Shur. Resonant detection of subterahertz radiation by plasma waves in a submicron field-effect transistor. *Applied Physics Letters*, 80, 2002.

[33] A. El Fatimya, F. Teppe, N. Dyakonova, and W. Knap. Resonant and voltage-tunable terahertz detection in ingaasinpingaasinp nanometer transistors. *Applied Physics Letters*, 89, 2006.

[34] Jian-Qiang Lu, M.S. Shur, J. L. Hesler, Liangquan Sun, and R. Weikle. Terahertz detector utilizing two-dimensional electronic fluid. *IEEE Electron Device Letters*, 19, 1998.

[35] Jian-Qiang Lu and M. S. Shur. Terahertz detection by high-electron-mobility transistor: Enhancement by drain bias. *Applied Physics Letters*, 78, 2001.

[36] W. Knap, F. Teppe, Y. Meziani, N. Dyakonova, and J. Lusakowski. Plasma wave detection of sub-terahertz and terahertz radiation by silicon field-effect transistors. *Applied Physics Letters*, 85, 2004.

[37] R. Tauk, F. Teppe, S. Boubanga, D. Coquillat, W. Knap, Y. Meziani, C. Gallon, F. Boeuf, T. Skotnicki, C. Fenouillet-Beranger, D. K. Maude, S. Rumyantsev, and M. S. Shur. Plasma wave detection of terahertz radiation by silicon field effect transistors: responsivity and noise equivalent power. *Applied Physics Letters*, 89, 2006.

[38] W. Knap et al. Field effect transistors for terahertz detection: Physics and first imaging applications. *Journal of Infrared, Millimeter, and Terahertz Waves*, 30:1319–1337, 2009.

[39] S. Komiyama, O. Astafiev, V. Antonov, T. Kutsuwa, and T. Hirai. A single photon detector in the far infrared range. *Nature*, 403:405–407, 2000.

[40] O. Astafiev, S. Komiyama, T. Kutsuwa, V. Antonov, Y. Kawaguchi, and K. Hirakawa. Single photon detector in the microwave range. *Applied Physics Letters*, 80:4250–4252, 2002.

[41] H. Hashiba, V. Antonov, L. Kulik, A. Tzalenchuk, P. Kleinschmidt, S. Giblin, and S. Komiyama. Isolated quantum dot in application to terahertz photon counting. *Physical review B*, 73:081310–1–081310–4, 2006.

[42] T. Ueda, Z. An, S. Komiyama, and K. Hirakawa. Charge-sensitive infrared phototransistors: Characterization by an all-cryogenic spectrometer. *Journal of Applied Physics*, 103:093109–1–093109–7, 2008.

[43] S. Komiyama. Single-photon detectors in the terahertz range. *IEEE Journal of selected topics in Quantum Electronics*, 17, 2011.

[44] R. J. Schoelkropf, S. H. Moseley, C. M. Stahle, P. Wahlgren, and P. Delsing. A concept for a submillimeter-wave single-photon counter. *IEEE Transactions on Applied Superconductivity*, 9:2935–2939, 1999.

[45] P. K. Day, H. G. LeDuc, B. A. Mazin, A. Vayonakis, and J. Zmuidzinas. A broadband superconducting detector suitable for use in large arrays. *Nature*, 425:817–821, 2003.

[46] J. Wei, D. Olaya, B. S. Karasik, S. V. Pereverzev, A. V. Sergeev, and M. E. Gershenson. Ultrasensitive hot-electron nanobolometers for terahertz astrophysics. *Nature Nanotechnology*, 3:496–500, 2008.

[47] M. A. Belkin et al. Terahertz quantum cascade lasers with copper metal-metal waveguides operating up to 178 k. *Optics Express*, 16:3242–3248, 2008.

[48] J. Grant et al. A monolithic resonant terahertz sensor element comprising a metamaterial absorber and micro-bolometer. *Laser and Photonics Reviews*, 7:1043–1048, 2013.

[49] I. E. Carranza, J. Grant, J. Gough, and D. R. S. Cumming. Metamaterial-based terahertz imaging. *IEEE Transactions on Terahertz Science and Technology*, 5:892 – 901, 2015.

[50] V. Dobrovolsky and F. Sizov. A room temperature, or moderately cooled, fast thz semiconductor hot electron bolometer. *Semiconductor Science and Technology*, 22:103, 2007.

[51] A. Kosarev et al. Sige:h-based micro-bolometers studied in the terahertz frequency range. *Solid State Electronics*, 54:417–419, 2010.

[52] F. Simoens and J. Lalanne-Dera. 36th int. conf. on infrared, millimeter and terahertz. pages 1–2, 2011.

[53] X. H. Lu et al . *Proceedings of SPIE*, 7277:72770N–7, 2008.

[54] F. Simoens and J. Meilhan. Terahertz real-time imaging uncooled array based on antenna- and cavity-coupled bolometers. *Philosophical Transactions of The Royal Society A Mathematical Physical and Engineering Sciences*, 372:1–12, 2014.

[55] S. Boppel et al. Ieee 12th topical meeting on silicon monolithic integrated circuits rf systems. volume SiRF 2012, pages 77–80, 2012.

[56] K. Ikushima, Y. Yoshimura, T. Hasegawa, S. Komiyama, T. Ueda, and K. Hirakawa. Photon-counting microscopy of terahertz radiation. *Applied Physics Letters*, 88:152110–1–1521103–3, 2006.

[57] K. Ikushima, H. Sakuma, Y. Yoshimura, S. Komiyama, T. Ueda, and K. Hirakawa. Thz imaging of cyclotron emission in quantum hall conductors. *Physica E*, 34:22–26, 2006.

[58] K. Ikushima, S. Komiyama, T. Ueda, and K. Hirakawa. Thz-photon generation due to electrons injected via quantum-hall edge channels. *Physica E*, 40:1026–1029, 2006.

[59] K. Ikushima, D. Asaoka, S. Komiyama, T. Ueda, and K. Hirakawa. Manipulating terahertz photons on a quantum hall effect device. *Physica E*, 42:1034–1037, 2010.

[60] S. Han, H. Ko, J. Park, N. Kim, Y. Yoon, J. Shin, D. Y. Kim, D. H. Lee, and K. H. Park. Ingaas schottky barrier diode array detector for a real-time compact terahertz line scanner. *Optics Express*, 21, 2013.

[61] D. Auston. Impulse response of photoconductors in transmission lines. *IEEE Journal of Quantum Electronics*, 19:639 – 648, 1983.

[62] Xiaoxia Yin, Brian Ng, and Derek Abbott. *Terahertz Imaging for Biomedical Applications*. Springer-Verlag New York, 1 edition, 2012.

[63] Martin van Exter, Ch. Fattinger, and D. Grischkowsky. Terahertz time-domain spectroscopy of water vapor. *Optics Letters*, 14:1128–1130, 1989.

[64] A. Cantor, P. Cheo, M. Foster, and L. Newman. Application of submillimeter wave lasers to high voltage cable inspection. *IEEE Journal of Quantum Electronics*, 17:477 – 489, 1981.

[65] W. He et al. Generation of broadband terahertz radiation using a backward wave oscillator and pseudospark-sourced electron beam. *Applied Physics Letters*, 107, 2015.

[66] N. G. Gavrilov et al. Status of the novosibirsk high-power terahertz fel. *Nuclear Instruments and Methods in Physics Research*, 575:54–57, 2007.

[67] A. Khalid et al. Terahertz oscillations in an in0.53ga0.47as submicron planar gunn diode. *Journal of Applied Physics*, 115:114502, 2014.

[68]

[69] F. C. Cruz, T. Giovana, F. L. Leverson, and N. C. Frateschi. Conference on microwave and optoelectronics. 2007.

[70] B. S. Williams, S. Kumar, Q. Hu, and J. L. Reno. High-power terahertz quantum-cascade lasers. *Electronics Letters*, 42:89–91, 2006.

[71] L. Lianhe et al. Terahertz quantum cascade lasers with ¿1 w output powers. *Electronics Letters*, 50:309–311, 2014.

[72] M. A. Belkin et al. Terahertz quantum cascade lasers with copper metal-metal waveguides operating up to 178 k. *Optics Express*, 16:3242–3248, 2008.

[73] M. Wienold et al. High-temperature, continuous-wave operation of terahertz quantum-cascade lasers with metal-metal waveguides and third-order distributed feedback. *Optics Express*, 22:3334–48, 2014.

[74] A. Wade et al. Magnetic-field-assisted terahertz quantum cascade laser operating up to 225 k. *Nature Photonics*, 3:41–5, 2009.

[75] M. Razeghi et al. Quantum cascade lasers: from tool to product. *Optics Express*, 23:8462–8475, 2015.

[76] Ping Gu, Fan Chang, Masahiko Tani, Kiyomi Sakai, and Ci-Ling Pan. Generation of coherent cw-terahertz radiation using a tunable dual-wavelength external cavity laser diode. *Japanese Journal of Applied Physics*, 38, 1999.

[77] I. S. Gregory, W. R. Tribe, B. E. Cole, C. Baker, M. J. Evans, I. V. Bradley, E. H. Linfield, A. G. Davies, and M. Missous. Phase sensitive continuous-wave thz imaging using diode lasers. *Electronics Letters*, 40:143 – 145, 2004.

[78] Rudeger Kohler, Rita C. Iotti, Alessandro Tredicucci, and Fausto Rossi. Design and simulation of terahertz quantum cascade lasers. *Applied Physics Letters*, 79, 2001.

[79] Rudeger Kohler, Alessandro Tredicucci, and Fabio Beltram. High-intensity interminiband terahertz emission from chirped superlattices. *Applied Physics Letters*, 80, 2002.

[80] L. Ozyuzer, A. E. Koshelev, C. Kurter, N. Gopalsami, Q. Li, M. Tachiki, K. Kadowaki, T. Yamamoto, H. Minami, H. Yamaguchi, T. Tachiki, K. E. Gray, W.-K. Kwok, and U. Welp. Emission of coherent thz radiation from superconductors. *Science*, 318:1291–1293, 2007.

[81] R. Klemm et al. Terahertz emission from the intrinsic josephson junctions of high-symmetry thermally-managed bscco microstrip antennas. The 2017 Cryogenic Engineering Conference and International Cryogenic Materials Conference (CEC-ICMC). CUED Publications database, 2017.

[82] Takanari Kashiwagi et al. A high-tc intrinsic josephson junction emitter tunable from 0.5 to 2.4 terahertz. *Applied Physics Letters*, 107, 2015.

[83] Toshimitsu Mochizuki, Akira Ito, Jonathon Mitchell, Hidetoshi Nakanishi, Katsuto Tanahashi, Iwao Kawayama, Masayoshi Tonouchi, Katsuhiko Shirasawa, and Hidetaka Takato. Probing the surface potential of oxidized silicon by assessing terahertz emission. *Applied Physics Letters*, 110, 2017.

[84] P. Tingzon, L. Lopez, N. Oliver, N. Cabello, A. Cafe, A. De Los Reyes, J. Muldera, E. Prieto, C. Que, G. Santos, M. Tani, A. Salvador, E. Estacio, and A. Somintac. Terahertz emission and photoluminescence of silicon nanowires electrolessly etched on the surface of silicon (100), (110), and (111) substrates for photovoltaic cell applications. *Photonics and Nanostructures - Fundamentals and Applications*, 24:1 – 6, 2017.

[85] S. M. Sze. *Semiconductor Devices*. WILEY, 2nd edition edition, 2002.

[86] John H. Davies. *The Physics of Low-dimensional Semiconductors*. Cambridge University Press, 2nd edition edition, 1997.

[87] Yuri M. Galperin. *Introduction to Modern Solid State Physics*. CreateSpace Independent Publishing Platform, 2014.

[88] A. Y. Cho. Film deposition by molecular-beam techniques. *Journal of Vacuum Science and Technology*, 8, 1971.

[89] Images courtesy of Patrick See., 2016.

[90] Tapash Chakraborty. Physics of the artificial atoms: Quantum dots in a magnetic field. *Comments on Condensed Matter Physics*, 16:35–68, 1992.

[91] V. Fock. Bemerkung zur quantelung des harmonischen oszillators im magnetfeld. *Zeitschrift für Physik*, 47:446–448, 1928.

[92] A history of the question: Can free electrons be polarized? *Historical Studies in the Physical Sciences*, 15:39, 1984.

[93] S. Debald and C. Emary. Spin-orbit-driven coherent oscillations in a few-electron quantum dot. *Physical Review Letters*, 94:226803, 2005.

[94] S. Debald. *Interaction and confinement in nanostructures: Spin-orbit coupling and electron-phonon scattering*. PhD thesis, Universität Hamburg, 2005.

[95] L. Landau. Diamagnetismus der metalle. *Zeitschrift für Physik*, 64:629–637, 1930.

[96] B. H. Bransden and C. J. Joachain. *Introduction to Quantum Mechanics*. Longman scientific and technical, 1990.

[97] L.P. Kouwenhoven, D.G. Austing, and S. Tarucha. Few-electron quantum dots. *Reports on progress in physics*, 64:701–736, 2001.

[98] Vyacheslavs Kashcheyevs and Bernd Kaestner. Universal decay cascade model for dynamic quantum dot initialization. *Physical Review Letters*, 104(186805), 2010.

[99] M. Kataoka, J.D. Fletcher, P. See, S.P. Giblin, T.J.B.M. Janssen, J.P. Griffiths, G.A.C. Jones, I. Farrer, and D.A. Ritchie. Tunable nonadiabatic excitation in a single-electron quantum dot. *Physical Review Letters*, 106, 2011.

[100] Private communications with Dr. Clive Emary., 2015.

[101] Ryan Jones, Reece Saint, and Beatriz Olmos. Far-field resonance fluorescence from a dipole-interacting laser-driven cold atomic gas. *Journal of Physics B: Atomic, Molecular and Optical Physics*, 50:014004, 2016.

[102] L. Allen and J. H. Eberly. *Optical Resonance and Two-Level Atoms.* Dover Publications, 1987.

[103] T. Fujisawa, D. G. Austing, Y. Tokura, Y. Hirayama, and S. Tarucha. Allowed and forbidden transitions in artificial hydrogen and helium atoms. *Nature*, 419:278–281, 2002.

[104] E. A. Zibik, T. Grange, B. A. Carpenter, N. E. Porter, R. Ferreira, G. Bastard, D. Stehr, S. Winnerl, M. Helm, H. Y. Liu, M. S. Skolnick, and L. R. Wilson. Long lifetimes of quantum-dot intersublevel transitions in the terahertz range. *Nature Materials*, 8:803–807, 2009.

[105] J. I. Climente, A. Bertoni, G. Goldoni, and E. Molinari. Phonon-induced electron relaxation in weakly confined single and coupled quantum dots. *Physical Review B*, 74:035313, 2006.

[106] Hai Wei, Ming Gong, Guang-Can Guo, and Lixin He. Atomistic theory of spin relaxation in self-assembled ingaas/gaas quantum dots at zero magnetic field. *Arxiv*, 2018.

[107] NPL. Courtesy of Dr. Masaya Kataoka, 2013.

[108] M. Büttiker, H. Thomas, and A. Prêtre. Mesoscopic capacitors. *Physics Letters A*, 180:364–369, 1993.

[109] S.P. Giblin, P. See, A. Petrie, T.J.B.M. Janssen, I. Farrer, J.P. Griffiths, G.A.C. Jones, D.A. Ritchie, and M. Kataoka. High-resolution error detection in the capture process of a single-electron pump. *Applied Physics Letters*, 108, 2016.

[110] J.D. Fletcher, M. Kataoka, S.P. Giblin, Sunghun Park, H.-S. Sim, P. See, D.A. Ritchie, J.P. Griffiths, G.A.C. Jones, H.E. Beere, and T.J.B.M. Janssen. Stabilization of single-electron pumps by high magnetic fields. *Physical review B*, 86, 2012.

[111] Myung-Ho Bae, Ye-Hwan Ahn, Minky Seo, Yunchul Chung, J.D. Fletcher, S.P. Giblin, M. Kataoka, and Nam Kim. Precision measurement of a potential-profile tunable single-electron pump. *Metrologia*, 52, 2015.

[112] J. Waldie, P. See, V. Kashcheyevs, J. P. Griffiths, I. Farrer, G. A. C. Jones, D. A. Ritchie, T. J. B. M. Janssen, and M. Kataoka. Measurement and control of electron wave packets from a single-electron source. *Physical Review B*, 92:125305, 2015.

[113] L. M. K. Vandersypen, J. M. Elzerman, R. N. Schouten, L. H. Willems van Beveren, R. Hanson, and L. P. Kouwenhoven. Real-time detection of single-electron tunneling using a quantum point contact. *Applied Physics Letters*, 85, 2004.

[114] Niels Ubbelohdeand Christian Fricke, Christian Flindt, Frank Hohls, and Rolf J. Haug. Measurement of finite-frequency current statistics in a single-electron transistor. *Nature Communications*, 3, 2012.

[115] O. Astafiev, V. Antonov, T. Kutsuwa, and S. Komiyama. Far-infrared spectroscopy of single quantum dots in high magnetic fields. *Physical Review B*, 65:085315, 2002.

[116] Courtesy of Dr. Vladimir Antonov., 2013.

[117] Confidential documentation provided by Vladimir Antonov., 2010.

[118] S. Pelling, R. Davis, L. Kulik, A. Tzalenchuk, S. Kubatkin, T. Ueda, S. Komiyama, and V.N. Antonov. Point contact readout for a quantum dot terahertz sensor. *Applied Physics Letters*, 93:073501, 2008.

[119] P. Kleinschmidt, S. Giblin, A. Tzalenchuk, H. Hashiba, V. Antonov, and S. Komiyama. Sensitive detector for a passive terahertz imager. *Journal of Applied Physics*, 99:114504, 2006.

[120] S. Pelling, Ernst Otto, S. Spasov, Sergey Kubatkin, R. Shaikhaidarov, K. Ueda, S. Komiyama, and V.N. Antonov. Electrostatic effects in coupled quantum dot-point contact-single electron transistor devices. *Journal of Applied Physics*, 112:014322, 2012.

[121] Kodo Kawase, Yuichi Ogawa, and Yuuki Watanabe. Non-destructive terahertz imaging of illicit drugs using spectral fingerprints. *Optics Express*, 11:2550, 2003.

[122] Peter Schemmel, Gilles Diederich, and Andrew J. Moore. Measurement of direct strain optic coefficient of ysz thermal barrier coatings at ghz frequencies. *Optics Express*, 25, 2017.

[123] J. Yun, D. Yoon, H. Kim, and J-S. Rieh. 300-ghz inp hbt oscillators based on common-base cross-coupled topology. *IEEE Transactions on Microwave Theory and Techniques*, 62:3053, 2014.

[124] T. M. Benseman, K. E. Gray, A. E. Koshelev, W.-K. Kwok, U. Welp, H. Minami, K. Kadowaki, and T. Yamamoto. Powerful terahertz emission from bi2sr2cacu2o8+ mesa arrays. *Applied Physics Letters*, 2013.

[125] R. Shaikhaidarov, V. N. Antonov, A. Casey, A. Kalaboukhov, S. Kubatkin, Y Harada, K. Onomitsu, A. Tzalenchuk, and A. Sobolev. Detection of coherent terahertz radiation from a high-temperature superconductor josephson junction by a semiconductor quantum-dot detector. *Physical Review Applied*, 5:024010, 2016.

[126] J. W. Song, N. A. Kabir, Y. Kawano, K. Ishibashi, G. R. Aizin, L. Mourokh, J. L. Reno, A. G. Markelz, and J. P. Bird. Terahertz response of quantum point contacts. *Applied Physics Letters*, 92:223115, 2008.

[127] J. W. Song, G. Aizin, Y. Kawano, K. Ishibashi, N. Aoki, Y. Ochiai, J. L. Reno, and J. P. Bird. Bolometric terahertz detection in pinched-off quantum point contacts. *Applied Physics Letters*, 97:083109, 2010.

[128] A.V. Muravjov, D. B. Veksler, V. V. Popov, O. V. Polischuk, N. Pala, X. Hu, R. Gaska, H. Saxena, R. E. Peale, and M. S. Shur. Temperature dependence of plasmonic terahertz absorption in grating-gate gallium-nitride transistor structures. *Applied Physics Letters*, 96:042105, 2010.

[129] A. El Fatimy, F. Teppe, N. Dyakonova, W. Knap, D. Seliuta, G. Valušis, A. Shchepetov, Y. Roelens, S. Bollaert, A. Cappy, and S. Rumyantsev. Resonant and voltage-tunable terahertz detection in ingaasinpingaasinp nanometer transistors. *Applied Physics Letters*, 89:131926, 2006.

[130] V. M. Muravev and I. V. Kukushkin. Plasmonic detector/spectrometer of subterahertz radiation based on two-dimensional electron system with embedded defect. *Applied Physics Letters*, 100:082102, 2012.

[131] L. Vicarelli, M. S. Vitiello, D. Coquillat, A. Lombardo, A. C. Ferrari, W. Knap, M. Polini, V. Pellegrini, and A. Tredicucci. Graphene field-effect transistors as room-temperature terahertz detectors. *Nature Materials*, 11:865–871, 2012.